Mammalian translation termination intermediates captured using PDMS microfluidics-based time-resolved cryo-EM (TRCEM)

Prikshat Dadhwal

Submitted in partial fulfillment of the
requirements for the degree of
Doctor of Philosophy
under the Executive Committee
of the Graduate School of Arts and Sciences

COLUMBIA UNIVERSITY

2024

Abstract

Mammalian translation termination intermediates captured using PDMS microfluidics-based time-resolved cryo-EM

Prikshat Dadhwal

Termination of translation in eukaryotes occurs when a translating ribosome encounters a stop codon (UAA, UAG, or UGA) in its A site. This triggers the recruitment of translation termination factors eRF1, a tRNA-mimicking protein responsible for decoding the stop codon and catalyzing peptide release, and eRF3, a translational GTPase that stimulates peptide release in a GTP-hydrolysis-dependent manner. Upon successful stop codon decoding by eRF1, eRF3 carries out GTP hydrolysis and dissociates from the ribosome. eRF1 subsequently gets accommodated into the peptidyl transferase center (PTC) and catalyzes the release of the nascent peptide [1-9]. The structures for the pre-accommodated eRF1 with eRF3 trapped on ribosome using non-hydrolysable GTP analogs as well as for the PTC-accommodated eRF1 have been solved using cryogenic electron-microscopy (cryo-EM) [3-6, 11, 12]. The structures reveal the binding mode and interactions between the release factors and the pre-termination complex. However, the mechanism of eRF3 GTPase activation and subsequent eRF1 accommodation into the PTC remains poorly understood. To address this knowledge gap, we used single-particle time-resolved cryo-EM (TRCEM) [13-23] to capture the structures of intermediates formed during the termination process.

For our TRCEM experiments, we first developed a Polydimethylsiloxane (PDMS)-based modular microfluidic mixing-spraying device with a SiO_2 internal coating. The device has a SiO_2-coated PDMS-based 3D splitting-and-recombination (SAR) micro-mixer capable of mixing

two fluids within 0.5 ms with more than 90% efficiency. The SiO_2 coating strengthens the PDMS channels and acts as a hydrophilic barrier preventing sample adsorption to the PDMS surface. The micro-mixer is connected to a glass microcapillary that acts as the reaction channel. Channels of different lengths can be used to vary the overall reaction time between 10 ms and 1000 ms. The microcapillary is connected to a 3D micro-sprayer for generating a 3D plume of sprayed droplets. A cryo-EM grid is passed through the spray cone to collect droplets and is rapidly plunged into liquid cryogen for vitrification.

By using TRCEM as well as the conventional blotting method for cryo-EM sample preparation, we captured the reaction between a pre-termination (pre-TC) mimic and the ternary complex of eRF1, eRF3, and GTP at reaction times of 450 ms, 900 ms, 15 s, and 10 min. Classification of the cryo-EM data resulted in maps for five distinct factor-bound classes. Four maps belonged to intermediates with densities for eRF1 and eRF3 bound to the pre-TC in varying conformations. The fifth map had a density matching the PTC-accommodated eRF1 [3]. Population analysis allowed us to arrange the classes chronologically and track the events leading to GTPase activation during the termination process. Atomic model building and refinement allowed us to determine the hydrolysis state of the eRF3-bound GTP and revealed the catalytic mechanism for GTP-hydrolysis. The models revealed a potential mechanism for GDP dissociation post-GTP-hydrolysis.

Table of Contents

List of Charts, Graphs, Illustrations

Chapter 1

Chapter 2

Chapter 3

Chapter 4

Acknowledgments

I would like to thank my mentor Joachim Frank for all his help and guidance throughout all these years. I want to thank my committee members Liang Tong and John F. Hunt for their guidance. Special thanks to Xiangsong Feng, whom I worked with extensively throughout my PhD for the development of the time-resolved method and for conducting experiments. Thank you for your intuitive ideas and suggestions. Gratitude to all the current and former members of the Frank lab: Swastik De, Sayan Bhattacharjee, Suvrajit Maji, Zuben P. Brown, Francisco Acosta-Reyes, Jack Fu, and Sandip Kaledhonkar. All of them helped me a lot during my stay at Columbia and for that I am grateful. I would also like to thank my collaborators Christopher U. T. Hellen, Tatyana V. Pestova, Qiao Lin, and Irina S. Abaeva. Your guidance and excellent-quality samples have played a big role in completing this work. Lastly, I would like to thank the members of the Columbia cryo-EM core Bob Grassucci, Zhening Zhang, and Harry Kao who trained me in cryo-EM and helped with the data collection.

Chapter 1: Proteins and the translation process

1.1 Proteins are versatile and essential components of cells

Proteins are essential macromolecules that play a critical role in cell function. With varying shapes and sizes, proteins perform a wide range of functions. As enzymes, they catalyze the creation and breakdown of diverse biomolecules. As transporters and channels, they help move materials across the cell membrane and maintain the proper concentration levels. As receptors and transcription factors, they form signaling networks that enable cells to respond to environmental signals and regulate specific genes. As microtubules and microfilaments, they provide structural support and transport within the cell. Despite their diversity in function, all proteins are formed in the same way by linking amino acids with peptide bonds. Twenty-one different amino acids are available for protein synthesis, leading to a vast array of protein sequences. After synthesis, proteins fold into specific 3D structures based on their sequence and length. The shape and mobility of the protein allow it to carry out its biological function [24].

1.2 Sequence information is passed from DNA to mRNA to protein

Genetic information is stored in Deoxyribonucleic acid (DNA) in the form of genes. These genes are composed of codon triplets that represent different amino acids. There are sixty-four distinct triplets, which code for twenty-one different amino acids and a stop signal. DNA-dependent RNA polymerase copies the genetic data during transcription, converting it into messenger Ribonucleic acid (mRNA). The ribosome, a complex molecular machine, uses the mRNA as a blueprint for synthesizing proteins in a process called translation. This process of

transferring information from DNA to mRNA to protein is the central dogma of molecular biology [25].

1.3 Ribosomes are molecular machines responsible for protein synthesis

Ribosomes are composed of a combination of protein and ribosomal RNA and have a consistent structure among different life forms. They consist of two subunits: the large subunit (LSU) and the small subunit (SSU) (**Figure 1**). They are known by their sedimentation coefficients in Svedberg units. The prokaryotic ribosome is known as 70S and includes 30S (SSU) and 50S (LSU) subunits. The eukaryotic ribosome is known as 80S and includes 40S (SSU) and 60S (LSU). The prokaryotic LSU is made up of two rRNA molecules (23S and 5S) and around 30 proteins, while the eukaryotic LSU is made up of three rRNA molecules (25S-28S, 5.8S, and 5S) and 46-47 proteins. The prokaryotic SSU comprises a single 16S rRNA and around 22 proteins, while the eukaryotic SSU comprises an 18S rRNA and around 33 proteins. Both subunits' rRNA is highly structured and mostly double-stranded, forming functionally important motifs. The LSU includes the peptidyl transferase center (PTC), where peptide bond formation occurs, the peptide exit tunnel from which the newly synthesized peptide chain exits, as well as the GTPase-associated center (GAC), and the Sarcin-Ricin loop (SRL), both of which play important roles in binding and activation of various translational guanosine triphosphatases (GTPases). The SSU has two noticeable parts called the head and body, which can move relatively. The mRNA encoding the protein is threaded between the two [28]. The SSU also has three distinct binding sites for transfer RNA (tRNA): the aminoacyl site (A site), the peptidyl site (P site), and the exit site (E site). The aminoacyl-tRNA first binds to the mRNA in the A site using its anticodon stem loop (ASL). The A site also includes the decoding center of the

ribosome consisting of a set of conserved bases that undergo conformational changes in response to proper codon-anticodon base pairing. After decoding, the aminoacyl end of the tRNA is accommodated into the PTC, where peptide bond formation occurs, and the newly formed peptide is transferred to the A-site tRNA. The peptidyl-tRNA is then moved from the A site to the P site and the deacylated tRNA is moved from the P site to the E site, from where it exits the ribosome [29-36]. The PTC's catalytic activity is carried out by rRNA alone, making the ribosome a true ribozyme [37]. The mammalian ribosome also contains a Z site for tRNA binding located downstream of the E site. The Z site is occupied by tRNA under normal growth conditions and its occupancy is increased under translational stress [26, 27]. The two subunits interact with each other through RNA-RNA, RNA-protein, and protein-protein interactions called inter-subunit bridges, some of which are broken and re-formed as the ribosome undergoes various conformational changes during the translation cycle [38].

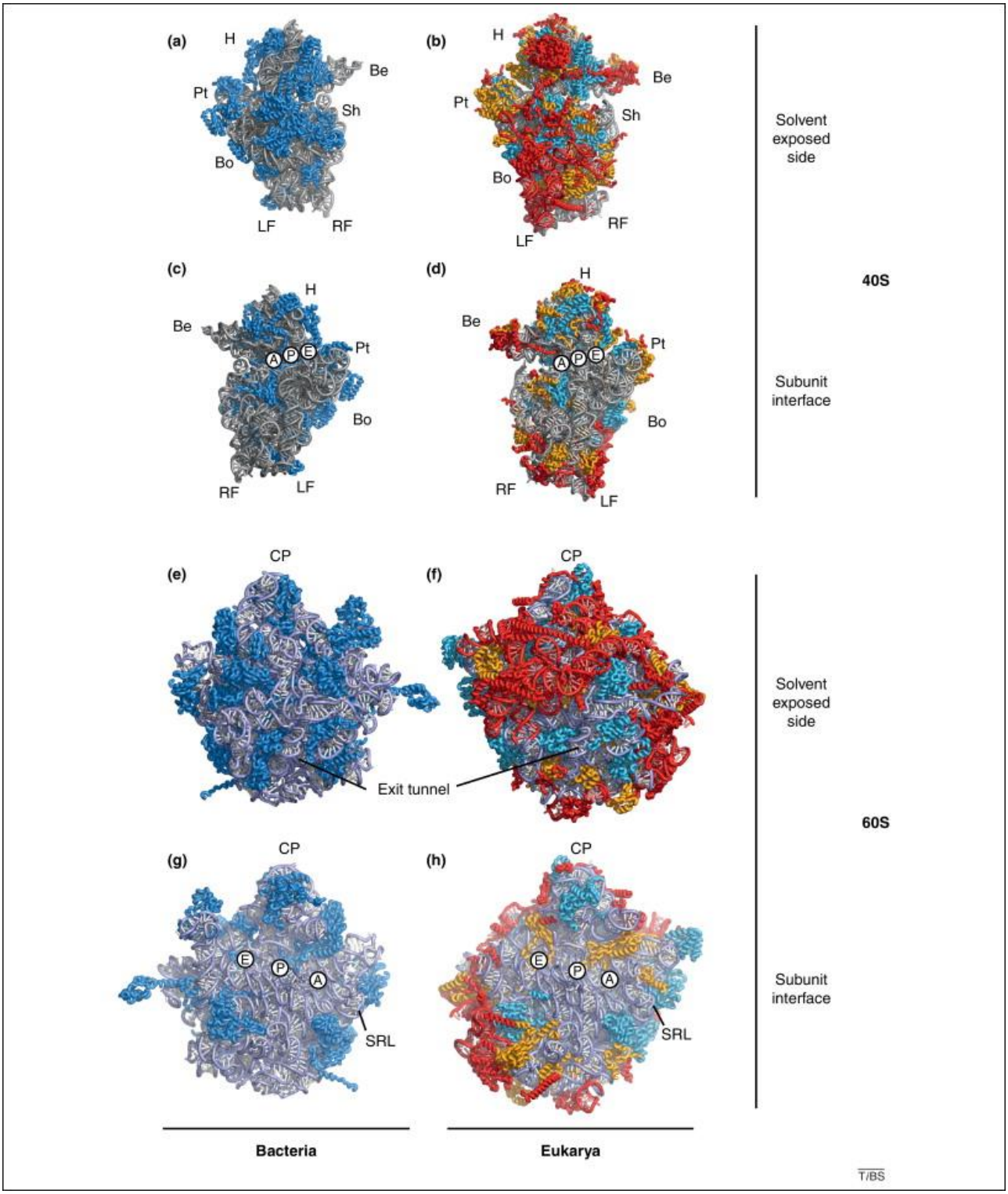
(a)
H
Be
Pt
Sh
Bo
LF
RF
(b)
H
Be
Pt
Sh
Bo
RF
LF
Solvent exposed side
(c)
H
Be
A
P
E
Pt
Bo
RF
LF
(d)
H
Be
A
P
E
Pt
Bo
RF
LF
Subunit interface
40S
(e)
CP
Exit tunnel
(f)
CP
Solvent exposed side
60S
(g)
CP
E
P
A
SRL
(h)
CP
E
P
A
SRL
Subunit interface
Bacteria
Eukarya
T/BS

Figure 1. Ribosomal subunits in prokaryotes and eukaryotes. a) and c) *Thermus thermophilus* 30S (PDB: 2J00), b) and d) *Tetrahymena thermophila* 40S (PDB: 2XZM), e) and g) *Thermus thermophilus* 50S (PDB: 2J01), and g) and h) *Tetrahymena thermophila* 60S (PDBs: 4A17 and 4A19). Universally conserved proteins are colored light blue; proteins specific to archaea and eukarya are colored gold; proteins and RNA elements specific to eukarya are colored red; and the rest are colored grey. SSU structures: head (H), beak (Be), platform (Pt), shoulder (Sh), body (Bo), left foot (LF), and right foot (RF). LSU structures: central protuberance (CP), sarcin-ricin loop (SRL), and protein exit tunnel. The A, P, and E sites on both subunits are marked with circles. Reprinted with permission from Elsevier, Klinge et al., 2012 [28]

1.4 The translation process

Translation involves dozens of protein and RNA factors and can be divided into four stages: initiation, elongation, termination, and recycling (**Figure 2**). It is a highly regulated process that is conserved across different kingdoms of life.

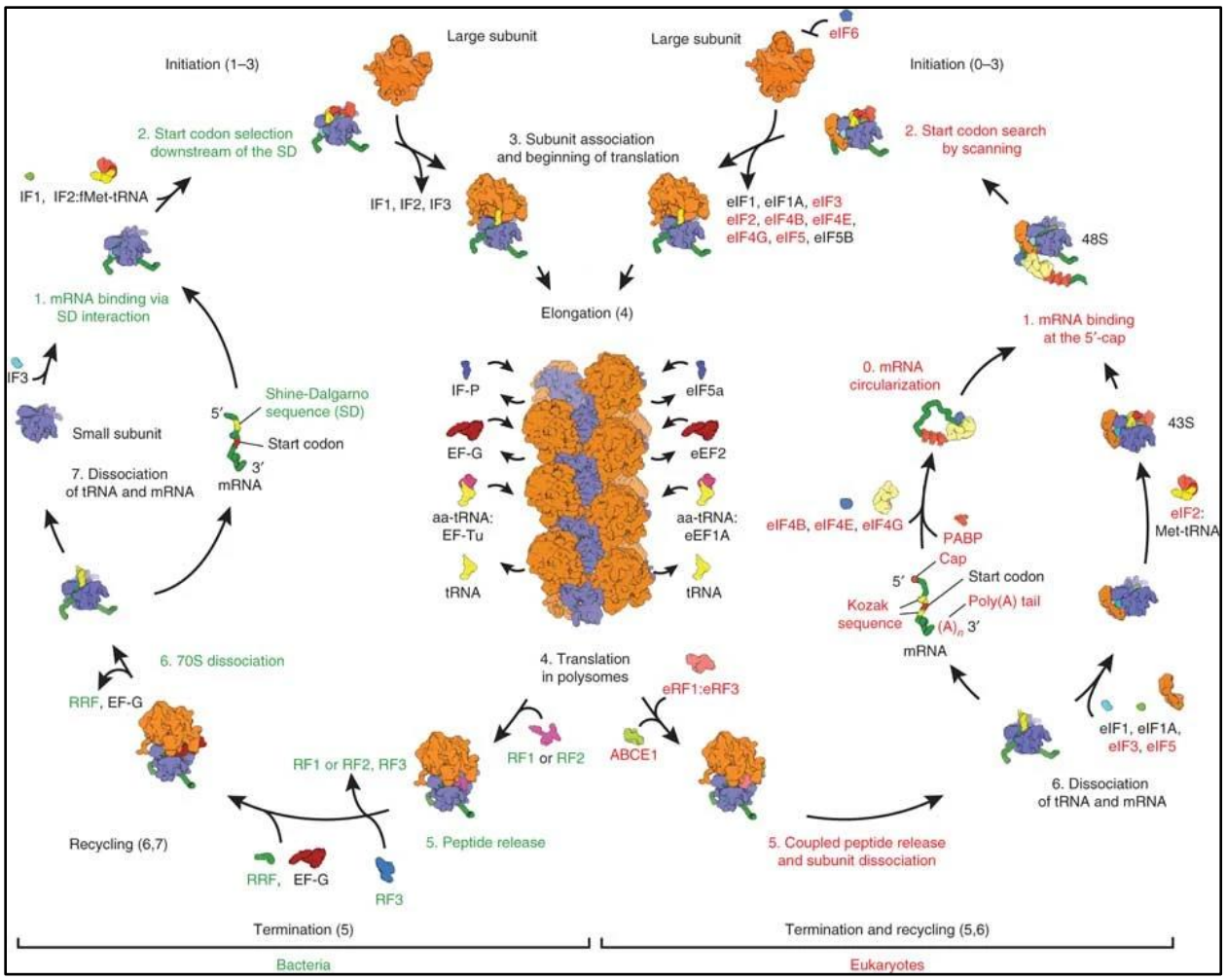

Figure 2. The translation process in prokaryotes and eukaryotes. Initiation factors (IFs in prokaryotes and eIFs in eukaryotes), elongation factors (EFs and eEFs), termination factors (RFs and eRFs), and recycling factors are depicted. Conserved steps and factors are depicted in black. Evolutionarily divergent steps and factors are colored green for prokaryotes and red for eukaryotes. Reprinted with permission from Springer Nature, Melnikov et al., 2012 [39]

1.5 Initiation of translation

The first step in protein synthesis is initiation, which is highly regulated and determines the rate of the process [40]. The goal of initiation is to position the initiator tRNA in the P site of

SSU, where it can base-pair with the start codon (AUG for canonical initiation) of the mRNA, and trigger the joining of the LSU. This creates the "elongation-competent" ribosome, which is ready for the next steps of translation. The initiation process differs between prokaryotes and eukaryotes, with eukaryotic initiation involving more protein factors and being more regulated (**Figure 2**). In addition to these processes, some viruses use a non-canonical initiation process called Internal Ribosomal Entry Site (IRES)-mediated initiation [41], which **we have used as a biochemical tool in our study.**

1.5.1 Initiation in Prokaryotes

In prokaryotes, translation initiation usually begins by binding of the SSU to the ribosome-binding site located in the 5' untranslated region (5'UTR) of mRNA. Most prokaryotic mRNAs contain an AG-rich sequence called the Shine-Dalgarno (SD) sequence [42] in their 5'UTR. This sequence is complementary to and base pairs with the anti-Shine-Dalgarno (aSD) sequence present on the 3'-end of the 16S rRNA in the SSU. This base pairing places the start codon near the P site of the SSU [43]. Some prokaryotic mRNAs contain 5'UTR that lacks the capacity to form stable SD-aSD pairing. Initiation for these mRNAs proceeds by a sequence non-specific binding of the SSU to the 5'UTR. The 5'UTR of non-SD-aSD paring mRNAs are often unstructured and the AUG start codon often resides in a single-stranded region facilitating SSU binding [43]. Another group of transcripts called 'leaderless' mRNA either completely lacks a 5'UTR or contains a short sequence (<8 nucleotides) upstream of the start codon [43]. The leaderless mRNA is capable of binding to both the SSU as well as the 70S ribosome [43], but the exact mechanism of initiation remains poorly understood. After locating the start codon, the binding and correct positioning of the initiator tRNA is facilitated by three different initiation

factors (IF1, 2, and 3). Once the initiator tRNA is properly positioned, the IFs leave and the LSU joins. This results in an elongation-competent complex that has an empty A site and is prepared for subsequent elongation cycles [39].

1.5.2 Initiation in eukaryotes

Eukaryotic mRNA does not contain the Shine-Dalgarno sequence for positioning the start codon near the P site. Therefore, the eukaryotic initiation complex needs to search for the start codon via a process called ‘scanning’. The eukaryotic mRNA has a 7-methylguanosine addition at its 5’-end, which is commonly known as the 5’-cap. This cap is crucial for the activation of mRNA during the initiation of translation. The eIF4F complex, comprising of eIF4E (cap-binding protein), eIF4A (RNA helicase), and eIF4G (scaffolding protein), binds to the 5’-cap. Moreover, eIF4G also binds to the poly-A binding protein (PABP) situated at the mRNA’s 3’-end, thereby bringing both ends together. This closed-loop mRNA is now primed for initiation.

To bind to the mRNA, the SSU must also be activated. The eukaryotic initiation factors eIF1, eIF1A, eIF5, and eIF3 initially bind to the SSU and prompt the binding of the ternary complex consisting of eIF2, GTP, and the initiator tRNA. This results in the formation of the 43S pre-initiation complex (PIC), which has an open mRNA channel and is prepared to bind to the activated mRNA.

After binding to the mRNA, the 43S-PIC initiates the scanning process. It searches for the start codon by scanning the 5' untranslated region (5'UTR) of the mRNA in the 5' to 3' direction. Once the initiator tRNA recognizes the start codon in the SSU P site, eIF2 hydrolyzes the bound GTP. This triggers conformational changes in the SSU, which lock the mRNA in place and help form the 48S initiation complex (48S IC). The 48S IC recruits the LSU with the

help of the checkpoint GTPase eIF5B. As the LSU is recruited, eIF1, eIF2-GDP, and eIF5 depart from the 48S IC. After a final conformation check carried out by eIF5B and eIF1A, the eIF5B-bound GTP is hydrolyzed, and the two proteins dissociate from the ribosome, resulting in the formation of an elongation-competent ribosome with an empty A site and a P-site tRNA [45, 46].

1.5.3 Internal ribosome entry site (IRES)-mediated initiation

In addition to the methods mentioned earlier, there are various non-canonical ways to start translation. IRES-mediated initiation is one such method. IRESs are RNA sequences that exist in either the 5'-UTR or the intergenic region of some positive-strand RNA viruses. These sequences have structural characteristics that allow them to begin translation on host ribosomes, without needing some or all of the initiation factors. IRESs are categorized into four types (I-IV) based on their structural complexity and the number of initiation factors required. Type I IRESs are the least structured and require the most initiation factors, while Type IV IRESs are the most structured and do not require any initiation factors to begin protein synthesis. Unlike Type I-III IRESs, Type IV IRESs do not start protein synthesis from an AUG start codon, but instead, use a non-AUG codon to start protein synthesis and move straight to the elongation phase [41].

We employ the Type IV IRES from the intergenic region of Halastavi árva virus (HalV) [33] to assemble ribosome complexes for our studies.

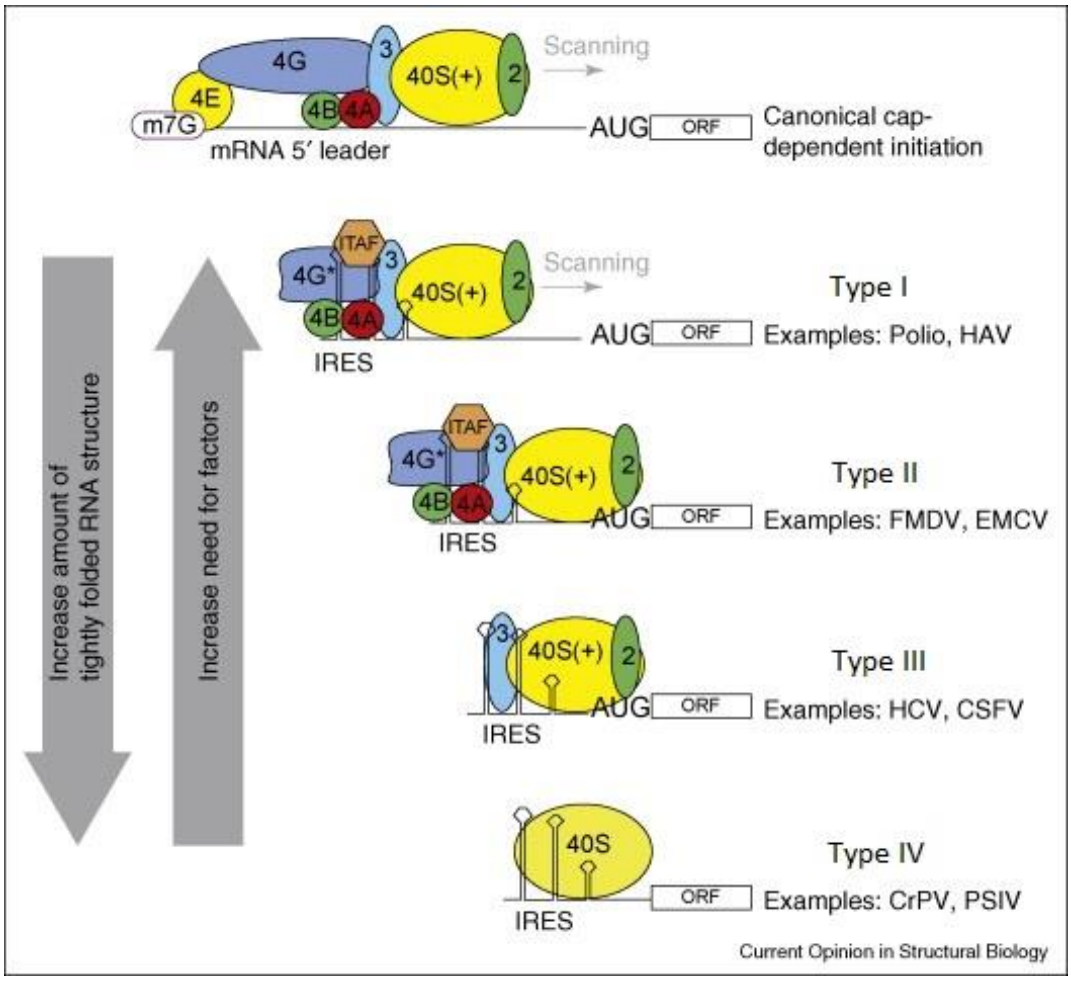

Figure 3. Factor requirements for canonical cap-dependent and IRES (Type I-IV) mediated translation initiation. Reprinted with permission from Filbin and Kieft [41].

1.6 Elongation of the polypeptide chain

Elongation follows initiation and is the most processive step of translation. It is a cyclical process involving the delivery of aminoacyl-tRNA to the ribosomal A site, a peptidyl transfer reaction to move the peptide chain to the A-site tRNA, and a translocation step to move the ribosome to the next codon. The elongation process is highly conserved between prokaryotes and eukaryotes and is carried out by homologous proteins [39]. Elongation begins with the delivery of the first aminoacyl-tRNA to the A site of an elongation-competent ribosome by GTPases --

EF-Tu in prokaryotes and eEF1A in eukaryotes -- in a ternary complex with GTP [48, 49]. The anticodon stem loop of the aminoacyl-tRNA interacts with the A-site codon in the decoding center of the ribosome. Successful decoding triggers GTP hydrolysis and eventual departure of EF-Tu/eEF1A and GDP-Pi from the ribosome. The aminoacyl end of the tRNA then gets accommodated into the PTC where the peptidyl transfer reaction takes place moving the peptide chain to the A-site tRNA. Translocation follows peptide transfer and is carried out by GTPases EF-G in prokaryotes and eEF2 in eukaryotes. EF-G/eEF2 partially insert into the A site on the LSU and interacts with the peptidyl-tRNA. The proteins act as molecular ratchets and move the ribosome on the mRNA by three nucleotides coupled with GTP hydrolysis. This also results in the movement of the peptidyl-tRNA to the P site and an empty A site ready for the next elongation cycle [34].

1.7 Termination of the translation

After several elongation cycles, the ribosome will eventually encounter one of three stop codons (UAA, UAG, or UGA), signaling the end of the mRNA coding region. When the stop codon enters the A site of the ribosome, translation termination is triggered. The termination process is facilitated by proteins known as termination or release factors (RFs). In both prokaryotes and eukaryotes, two classes of RFs exist class I and class II. Class I RFs act as tRNA substitutes, responsible for decoding the stop codon and catalyzing peptide release. Class II RFs are GTPases, and their function differs between prokaryotes and eukaryotes [1-12].

1.7.1 Termination of translation in prokaryotes

Prokaryotes have two class I RFs, namely RF1 and RF2. Both RFs can recognize the UAA codon whereas the UAG and the UGA codons are uniquely recognized by RF1 and RF2, respectively. Class I RFs consist of four domains: Domain 1 is responsible for binding to the L11 stalk of LSU and the class II release factor, Domains 2 and 4 together form a super domain responsible for stop codon recognition, and Domain 3 contains the catalytic GGQ motif responsible for catalyzing peptide release. The process has been studied extensively using biochemical, biophysical, and X-ray crystallographic studies. With the addition of recent studies with time-resolved cryo-EM, we have an almost complete picture of the termination process in prokaryotes [49].

RF1 and RF2 adopt a compact conformation in solution, where the catalytic domain harboring the GGQ motif is packed against the codon recognition domain. The RFs initially bind to the ribosome in this compact form. The universally conserved nucleotides of the decoding center - G530, A1493, and A1493 in E. coli 16S - play an important role in stop codon decoding and RF activation. They interact with the flexible switch loop (~290-305 in RF1 and ~310-325 in RF2) of the RFs and adopt a termination-specific conformation. This triggers the extension of the GGQ harboring domain 3 into the PTC. The GGQ motif catalyzes the hydrolysis of the ester bond between the nascent peptide and the P-site tRNA [49, 50].

After peptide release, the class I RFs dissociate from the ribosome. The dissociation is facilitated by the class II release factor RF3. RF3 is a GTPase homologous to EF-G and binds to the post-peptide release complex along with GDP. After binding, the GDP is exchanged with GTP resulting in conformational changes in RF3 as well as the ribosome. RF3-GTP stabilizes the ribosome in a rotated state and facilitates the release of class I RFs. RF3 then hydrolyses the GTP

and dissociates as well. Notably, RF3 is not conserved in prokaryotes and is non-essential for E. coli. This suggests that the release of the class I RFs is more dependent on ribosome rearrangement than on RF3 [50, 51].

1.7.2 Termination of translation in eukaryotes

Eukaryotic translation termination differs significantly from prokaryotic termination and is the primary focus of this work. Eukaryotes possess only one class I release factor named eRF1, which decodes all three stop codons. eRF1 is evolutionarily unrelated to the prokaryotic class I release factors and has a different domain architecture. eRF1 has three domains: the N-terminal domain (NTD) decodes the stop codon, the middle (M) domain catalyzes the hydrolysis of the ester bond between the nascent peptide and the tRNA, and the C-terminal domain (CTD) interfaces with the class II release factor eRF3, the GAC, and the SSU head (**Figures 4B and 5**). The NTD contains the conserved TASNIKS motif (residues 58-64 in human eRF1) which decodes the stop signal. Two additional motifs YxCxxxF (125-131) and GTS (31-33) help distinguish the +2 and +3 purine bases of the stop codon. Additionally, E55 helps distinguish UGG, which codes for tryptophan, from the stop codons. The M domain contains the conserved GGQ motif responsible for the catalysis of peptide release. The GGQ motif is held by eRF3 in an inactive state upon initial binding to the ribosome and is accommodated into the PTC only upon successful decoding of the stop codon. The CTD contains a mini domain (residues 328-373 in humans) that interacts with the N terminus of the ribosomal protein eS31. Mutations in the mini domain have been shown to increase termination readthrough of the UAG stop codon [1, 3, 11, 12, 52, 53, 54].

Eukaryotic class II release factor eRF3 is a GTPase homologous to elongation factors EF-Tu and eEF1A. eRF3 consists of three structured C-terminal domains (domain II, domain III, and G-domain) and an unstructured N-terminal region (**Figure 4A**). The latter is dispensable for the termination of translation. The function of eRF3 is significantly different from the prokaryotic RF3. eRF1 exists in solution in an extended conformation making it incompatible with binding to the ribosome. eRF3 acts as a chaperone and induces the compaction of eRF1, making it capable of binding to the pre-termination ribosome. In this way, eRF3 promotes the peptide release activity of eRF1 and makes the process GTP hydrolysis dependent [2, 4-12, 34, 55].

The release factors bind to the ribosome in a ternary complex with GTP. The two release factors form extensive contact with each other. The β7-α5 loop in the M domain of eRF1 binds the cleft between the G domain and domain 2 of eRF3 and directly interacts with the switch 1 and switch 2 regions [8]. Additionally, the helices α9, α12, and beta-strand β10 in the CTD of eRF1 interface with the loops connecting the beta strands β13- β14 and β15-16 in the domain 3 of eRF3 [8]. Upon binding, the eRF1 NTD reaches into the ribosomal A site and decodes the stop codon. Successful decoding triggers GTP hydrolysis by eRF3 and its eventual departure. Following this, eRF1 gets accommodated into the PTC and cleaves the ester bond between the nascent peptide and the P-site tRNA (**Figure 5A**). Unlike in prokaryotic termination, the eukaryotic class I release factor remains bound to the ribosome for the subsequent recycling step [3, 11, 34, 58].

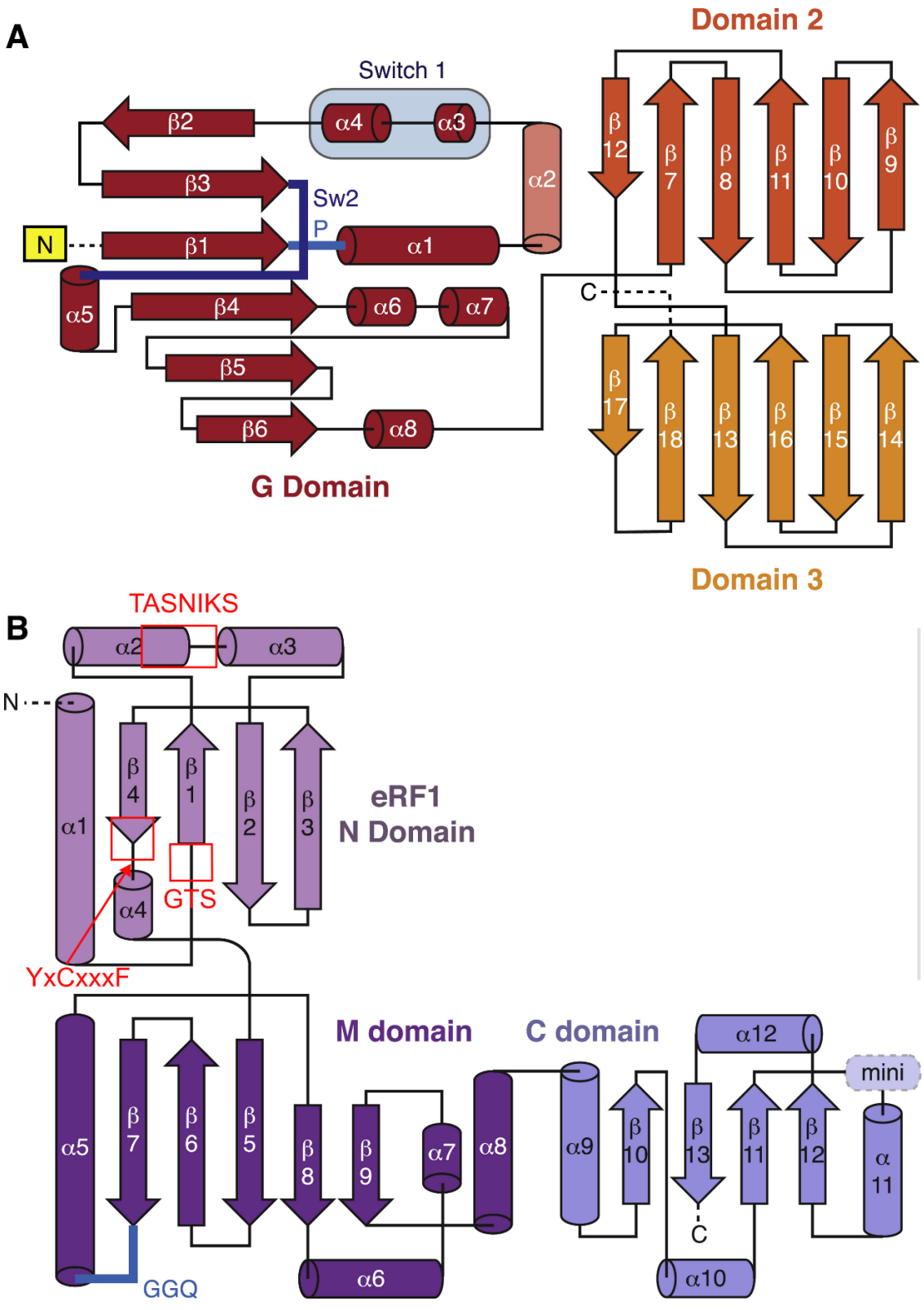
A
Domain 2
Switch 1
β2
α4
α3
α2
β3
Sw2
P
N
β1
α1
α5
β4
α6
α7
β5
β6
α8
C
G Domain
β 12
β 7
β 8
β 11
β 10
β 9
β 17
β 18
β 13
β 16
β 15
β 14
Domain 3
B
TASNIKS
α2
α3
N
α1
β 4
β 1
β 2
β 3
eRF1
N Domain
GTS
α4
YxCxxxF
M domain
C domain
α12
mini
α5
β 7
β 6
β 5
β 8
β 9
α7
α8
α9
β 10
β 13
β 11
β 12
α 11
C
GGQ
α6
α10

Figure 4. Secondary structure and domain architecture of eukaryotic release factors and homologous proteins. A) Domain architecture for translational GTPases eRF3 and eEF1A showing the homologous G-domain (red) and the two β-barrel domains (yellow and orange). Motifs important for GTP hydrolysis (switch 1, switch 2 (Sw 2), and P loop) are marked.

B) Domain architecture for decoding protein eRF1. The key motifs for stop codon recognition (TASNIKS, GTS, and YxxCxxxF) and the catalytic GGQ motif are indicated. Adapted from Shao et al., 2016 [8].

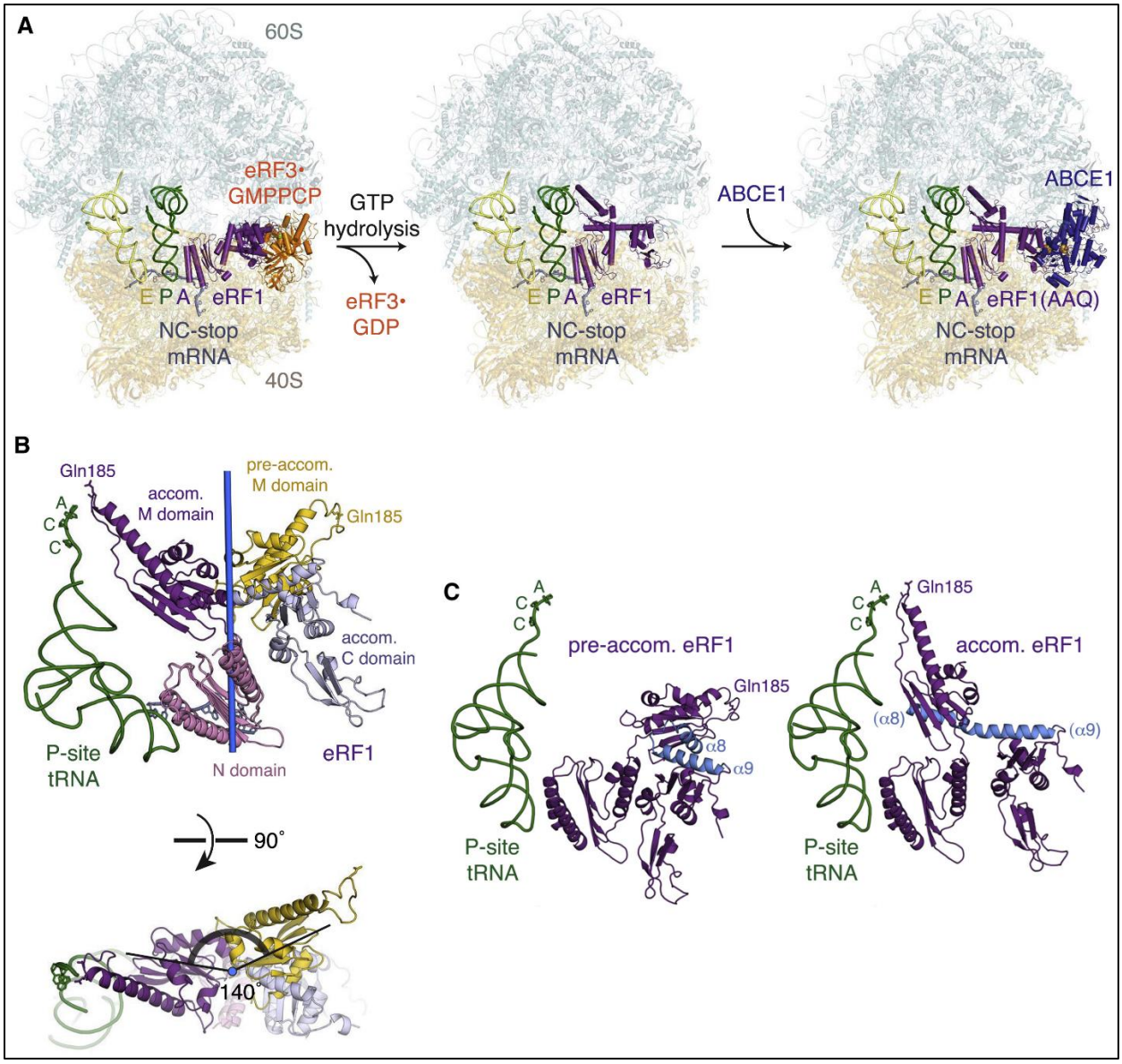

Figure 5. Accommodation process during eukaryotic translation termination and ribosome rescue. A) Structures for the eukaryotic termination complexes depicting the mechanism for eRF1 accommodation into the PTC. B) Comparison of the compact and extended conformations of eRF1 from the pre-accommodated and post-accommodated structures. C) and D) Side-by-side comparison of the pre-accommodated and post-accommodated states of eRF1. Adapted from Shao et al., 2016 [8]

1.8 Recycling of the ribosomes

Following peptide release, the ribosomes need to be recycled for performing subsequent protein synthesis. The process is quite different between prokaryotes and eukaryotes. In prokaryotes, recycling starts after dissociation of the release factors, whereas in eukaryotes the class I release factor remains bound and participates in the recycling process (**Figure 2**).

1.8.1 Ribosome recycling in prokaryotes

The prokaryotic post-termination complex consists of a ribosome bound to mRNA with a deacylated tRNA in the P site and an empty A site. This complex needs to be disassembled for recycling of ribosomes and the disassembly is carried out by the ribosome recycling factor (RRF) with help from EF-G. RRF is similar in shape and size to a tRNA and binds the A site. EF-G binds the inter-subunit space and partially inserts into the A site. The two proteins displace the tRNA from the P site and carry out GTP hydrolysis-dependent splitting of the ribosome into its subunits [56]. IF3 then binds to the SSU, preventing its reassociation with the LSU till the next round of initiation [57].

1.8.2 Ribosome recycling in eukaryotes

The eukaryotic post-termination complex has the class I release factor eRF1 still bound with a P-site deacylated tRNA and an mRNA. eRF1 facilitates ribosome recycling by recruiting the adenosine triphosphatase (ATPase) ABCE1(ATP-binding cassette sub-family E member 1) (**Figure 5A**) [58]. ABCE1 contains two nucleotide-binding domains (NBDs) that dimerize upon binding two ATP molecules. It also contains an N-terminal iron-sulfur (FeS) cluster domain, containing two $[4Fe\text{-}4S]^{2+}$ clusters as well as a conserved helix-loop-helix (HLH) motif [3].

ABCE1 binds to the ribosome and interfaces eRF1 in a semi-closed dimeric form along with two ATP molecules. ABCE1 hydrolyzes the ATP and adopts a closed conformation upon recognizing a splitting competent post-termination complex. This displaces the FeS domain towards eRF1 and triggers subunit splitting [59]. After splitting, ABCE1 remains bound to the SSU preventing its rejoining with the LSU. Additionally, ABCE1 has also been proposed to play a role in initiation, thereby linking the last step of translation to the first one [60-62].

Chapter 2: Introduction to single-particle TRCEM sample preparation

2.1 Cryo-EM is a method for high-resolution structure determination

Single-particle cryo-EM has become the method of choice for high-resolution biomolecular structure determination over the past couple of decades. The technique had been in development for many decades but was overshadowed by X-ray crystallography and Nuclear Magnetic Resonance (NMR), which provided higher-resolution information. Despite yielding lower resolution, cryo-EM still had its advantages. Unlike X-ray crystallography, cryo-EM does not require the crystallization of biomolecules, and unlike NMR, it is not limited to small proteins. This allows cryo-EM to apply to a wider variety of biomolecular targets. The main development that catapulted cryo-EM to be the mainstream structure determination method was the Direct Electron Detectors (DED) [63-66]. Before DEDs, the images were collected either on film or charge-couple device (CCD)/complementary metal-oxide semiconductor (CMOS) cameras. Both resulted in images with significant background noise and low signal, in addition to blurring due to sample motion during the exposure [67-69]. DEDs not only collect images with a better signal-to-noise ratio (SNR), but their high frame rates also allow for capturing multi-frame movies [70, 71]. The movie frames can then be aligned to compensate for sample drift during the exposure, a procedure termed ‘motion correction’ [72, 73]. The improved capabilities of the hardware were combined with the development of better software. The high-resolution capabilities of cryo-EM and the improved availability of high-end microscopes and better software have contributed significantly to making cryo-EM the technique of choice for biomolecular structure determination at atomic resolution [74].

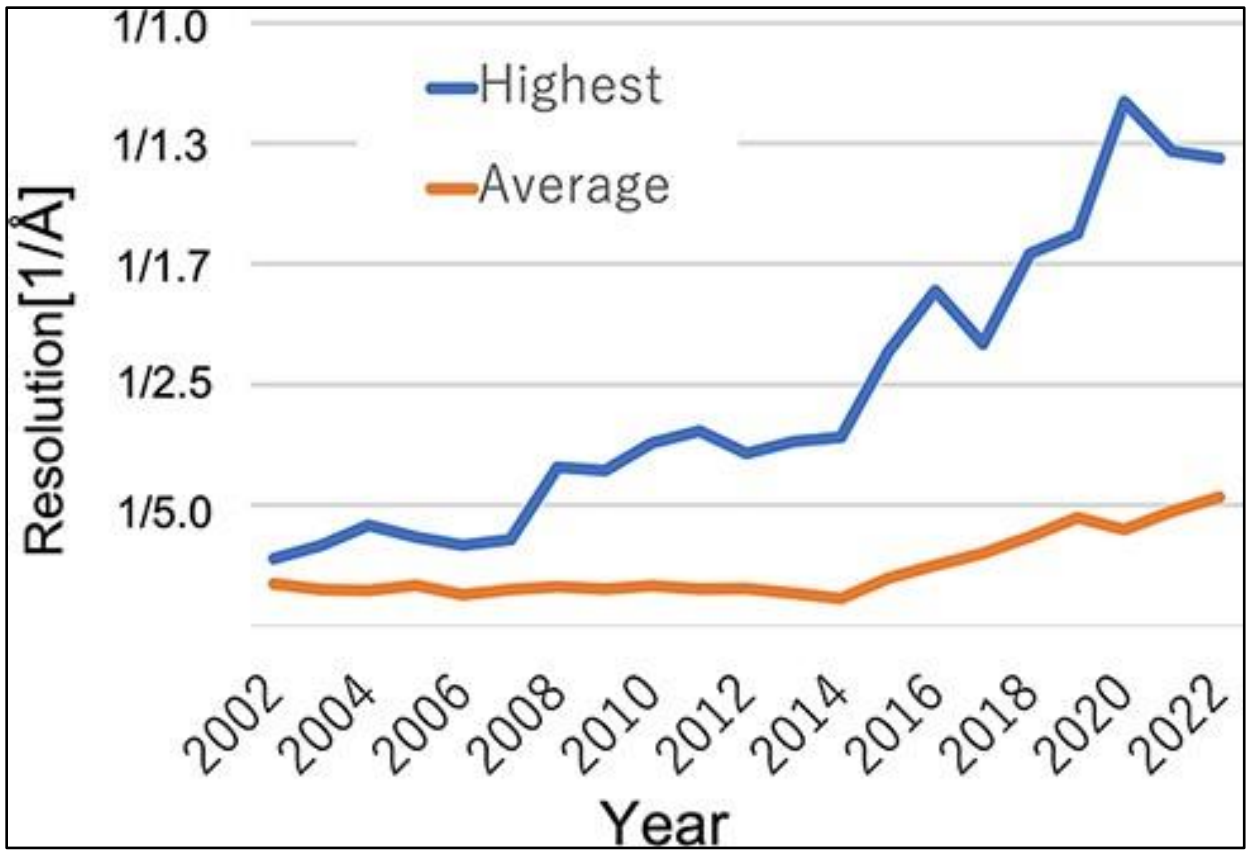

Figure 6. Trend of the highest and average resolution for structures solved by single-particle cryo-EM. Reprinted with permission from Oxford University Press, Fukuda et al., 2022 [74]

2.2 Sample preparation is limiting for capturing intermediate structures

Sample preparation for single particle cryo-EM involves the application of a few microliters of sample onto a cryo-EM grid followed by blotting to remove excess liquid, leaving behind a thin (~100 nm) film with a single layer of biomolecules. The grid is subsequently plunged into liquid ethane for rapid vitrification, trapping the biomolecules in a frozen-hydrated state (**Figure 7**) [75]. The process usually takes multiple seconds from initial application to freezing and the sample often reaches thermodynamic equilibrium by the time it is frozen. At thermodynamic equilibrium, most of the biomolecules occupy low energy states at the end of

their work cycles. Most high-energy states relevant for function are already depleted to a small fraction of the overall population [76]. This makes it difficult to study these high-energy states and it often requires the collection of large amounts of data to reach high resolution for these low-population states, making the process expensive in both instrument and computational times. The high-energy states are important to gain a full understanding of a biochemical system and are often good targets for therapeutic interventions. Many of these functionally-relevant high-energy intermediates have lifetimes on the millisecond time scale [76]. Therefore, trapping them requires fast sample preparation methods with precise control of reaction times.

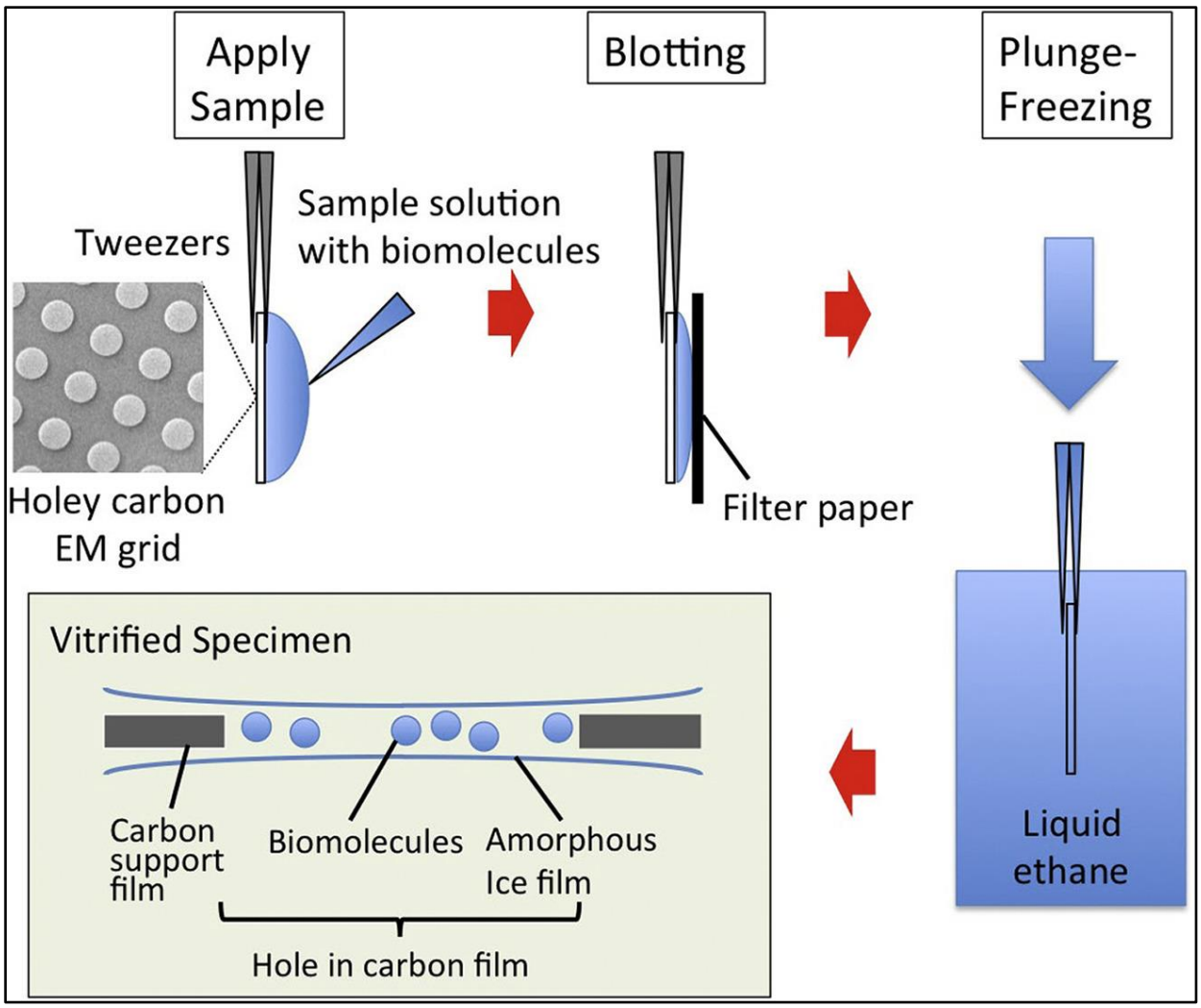

Figure 7. Sample preparation for single-particle cryo-EM by the conventional blotting method. From Murata and Wolf, 2018 [75]

2.3 TRCEM methods allow the capturing of intermediates

The low population of high-energy intermediates at thermodynamic equilibrium makes it difficult to obtain high-resolution structures and adds high cost in terms of instrument and computational time. To tackle this problem, TRCEM sample preparation methods have been developed [13-23]. TRCEM methods allow for capturing biochemical reactions in a pre-equilibrium state by controlling the total reaction time before vitrification. If the kinetics of a

biochemical reaction are known, the time points can be chosen such that the intermediates of interest are most abundant [77]. Thus, TRCEM provides access to information about biochemical reactions that is inaccessible by conventional methods [23].

2.4 TRCEM sample preparation has three steps

Much like time-resolved methods in other biochemical fields, TRCEM has three main steps: 1) Initiation of reaction, 2) Incubation of reaction, and 3) Sample application and quenching. All three are discussed below.

2.4.1 Initiation of reaction

The first step for TRCEM sample preparation is the initiation of the biochemical reaction quickly and synchronously. This is often achieved by mixing the two reaction components. This can be done by hand via pipetting, but this is only applicable to slow reactions. Mixing by hand has been employed in many past studies and **we have also employed it for part of this work**. For reactions on the millisecond time scale, faster mixing methods are required. The diffusion rate of proteins is in the order of 100 $\mu m^2 s^{-1}$ [78], which means diffusion alone is insufficient to achieve efficient mixing of reactions faster than a second (**Figure 8a**). Effective mixing is often achieved by reducing the distance that the two reacting species have to diffuse. This is done by increasing the contact surface and reducing the contact layer thickness between the two species. Fast mixing approaches can be categorized into two types: mixing post-application and mixing pre-application.

Mixing post-application involves on-grid mixing of the reactants after sequential application. One approach to do this involves the application and blotting of the first reactant on

the grid followed by plunging the grid through an aerosol containing the second reactant. This approach was used to study ATP-dependent activation of myosin on actin fibers and acetylcholine-dependent relaxation of the acetylcholine receptor [17, 79]. The mixing depends on the film thickness and the diffusion rates of the molecules employed. The approach is therefore limited to the study of interactions between biological macromolecules with small molecules, as larger molecules have much slower diffusion rates. A more recent approach for on-grid mixing TRCEM is employed in the Spotiton system [80]. The approach involves sequential application of the two reactants using two independent piezoelectric dispensers (**Figure 8b**). Spotiton uses special nanowire grids, with copper nanowires grown on the grid mesh. The nanowires wick away excess fluid from the grid squares resulting in the formation of thin layers. The thin layers allow for rapid mixing of the two reactants on the grid. The method has been used to study the structural dynamics of molecules like the ion channel MthK, RNA polymerase, and dynamin [81].

Mixing pre-application is a method in which the mixing of the reactants takes place before application to the grid. The mixing is often carried out using microfluidic mixers. Initial designs employed simple T-mixers that relied on diffusion across a single contact surface for mixing (**Figure 8c**) [82]. The T-mixers have low mixing efficiency at low flow rates and were replaced by more complex mixer geometries in later works. One such mixer was the planar butterfly mixer which achieved mixing by splitting and re-merging fluid streams multiple times to increase the fluid contact surface and reduce the diffusion layer thickness [16, 21, 22]. More recently, mixers with complex 3D geometries have been developed that achieve high mixing efficiency even at low flow rates (**Figure 8d**) [19]. The material used for constructing the micromixers has also changed significantly. Earlier methods used either glass or silicon [16, 21,

22] for fabricating micromixers, both of which require specialized equipment, training, and handling of hazardous chemicals. More recent methods have switched over to using elastic polymers, particularly Polydimethylsiloxane (PDMS), for fabricating the micromixers, making the process much simpler and cost-effective [19, 20, 23].

Another method for reaction initiation applies to specific photo-activated processes and ligands. The process involves the application and blotting of a pre-mixed sample containing an inactive reactant or a caged ligand onto a cryo-EM grid. The reaction is then started by flashing a light thereby activating the reactant or releasing the ligand. The reaction time in this case depends on the plunging delay [83-86].

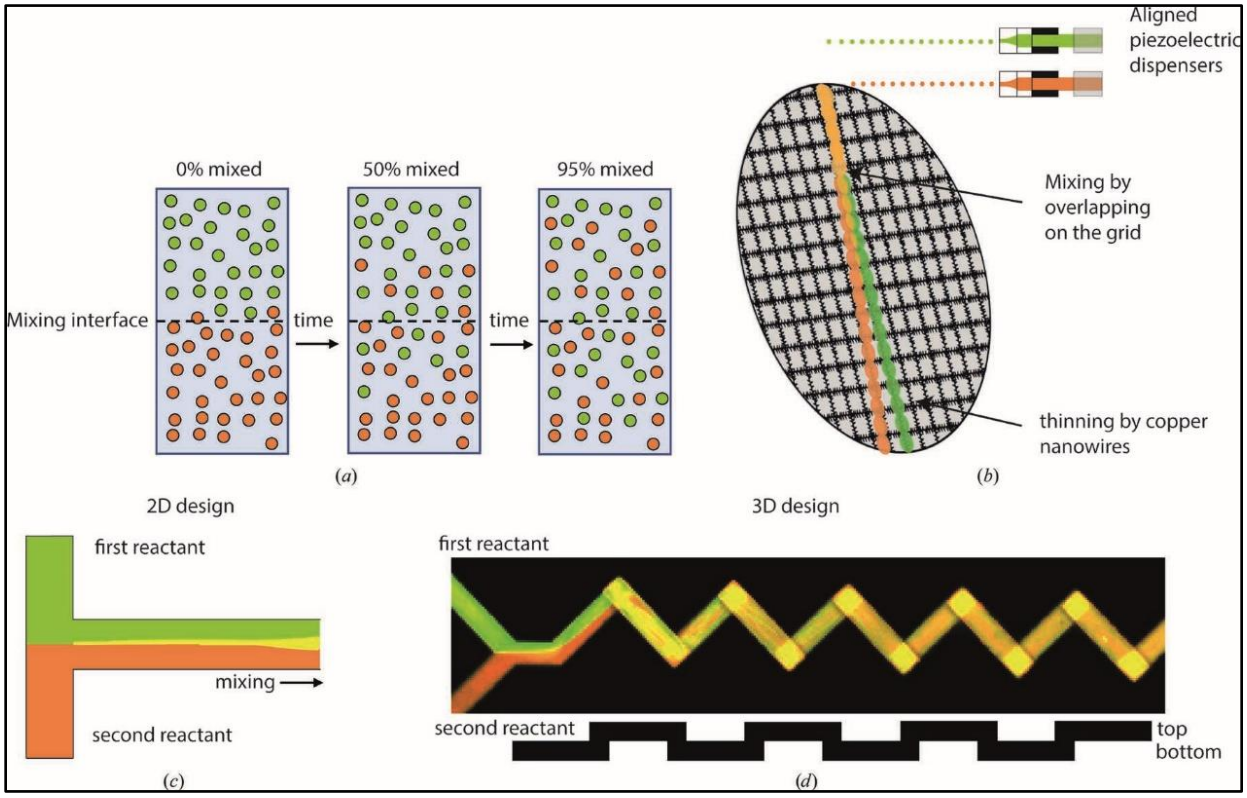

Figure 8. Overview of sample mixing. a) Depiction of diffusive-mixing of two species over time. b) On-grid mixing by sequential application of reactants using piezoelectric dispensers. The

mixing occurs in the overlapping regions. c) Parallel lamination mixing using a T-mixer. Mixing occurs primarily through diffusion at the interface of the two fluids. d) Mixing in a 3D micromixer by repeated breaking and re-merging of fluid streams. From Maeots and Enchev, 2022 [23].

2.4.2 Incubation of reaction

After efficient mixing, the reaction needs to be propagated for a fixed amount of time to maximize the population for the intermediate of interest. For slow reactions, this process is often performed in a test tube before sample preparation by the conventional blotting method [87,88]. For the mixing post-application case, the reaction takes place on the grid itself and the reaction time can be controlled by controlling the delay before plunge freezing. Although it seems simple, the caveat is that the reaction takes place in a thin layer of liquid and the reactants are exposed to the air-water interface. Interactions with the air-water interface can affect the kinetics of the reaction and potentially introduce artifacts in the structures obtained [89, 90].

For the mixing pre-application approach, the incubation time depends on the time it takes from mixing the reactant to the freezing of the sample. This includes the time for mixing, any dead time involved in sample application post-mixing, and the time it takes to plunge freeze the sample. The fastest times achievable by this method fall in the 10 ms time frame. For longer reaction times, additional delay can be added usually by extending the fluid path after the micromixer [16, 19, 21, 22]. Since a constant fluid flow rate is used for micro-mixing, the residence time inside the delay line can be calculated precisely by taking the ratio of the volume of the delay line to the liquid flow rate. The residence time calculated in this manner is the average residence time and is not reflective of the actual residence time of the reactants in the channel. This happens because, under laminar flow conditions, the fluid velocity within the

channel varies depending on the distance from the channel walls. The fluid flowing closer to the walls slows down whereas the fluid towards the center of the channel speeds up. This results in a discrepancy in the residence time of reactants close to the walls as compared to reactants towards the center of the channel. This effect becomes even worse for longer incubation times [19, 20, 23]. Experimental methods remain to be developed to overcome this issue.

2.4.3 Sample application and quenching

The final step of TRCEM sample preparation is the application of the reaction mixture to a cryo-EM grid followed by plunge freezing into liquid cryogen. Sample application is an important part of the TRCEM sample preparation process and often governs the quality of data obtainable. Single particle cryo-EM requires a monodispersed sample in a thin layer of vitrified ice to achieve good results. Many of the approaches involving mixing in a test tube or on-grid-mixing use the conventional blotting method for achieving good ice thickness [87-88], but this is not feasible for some of the faster TRCEM approaches. Droplet-based sample application is the most common approach for fast TRCEM sample preparation. The droplet-based methods produce droplets by using atomizers [17, 79], electrospray nozzles [82], gas-assisted nozzles [16, 18, 19, 22, 91], or piezoelectric nozzles [80, 81] (**Figure 9**). The droplets vary in size depending on the nozzle type used and are projected directly onto the grid. Blotting is unnecessary for droplets in the 10 μm size range, making the process much faster. The droplets spread out on the hydrophilic grid surface resulting in thin edges suitable for cryo-EM data collection. After spraying, the grid is rapidly plunge-frozen into liquid cryogen and stored under liquid nitrogen before data collection.

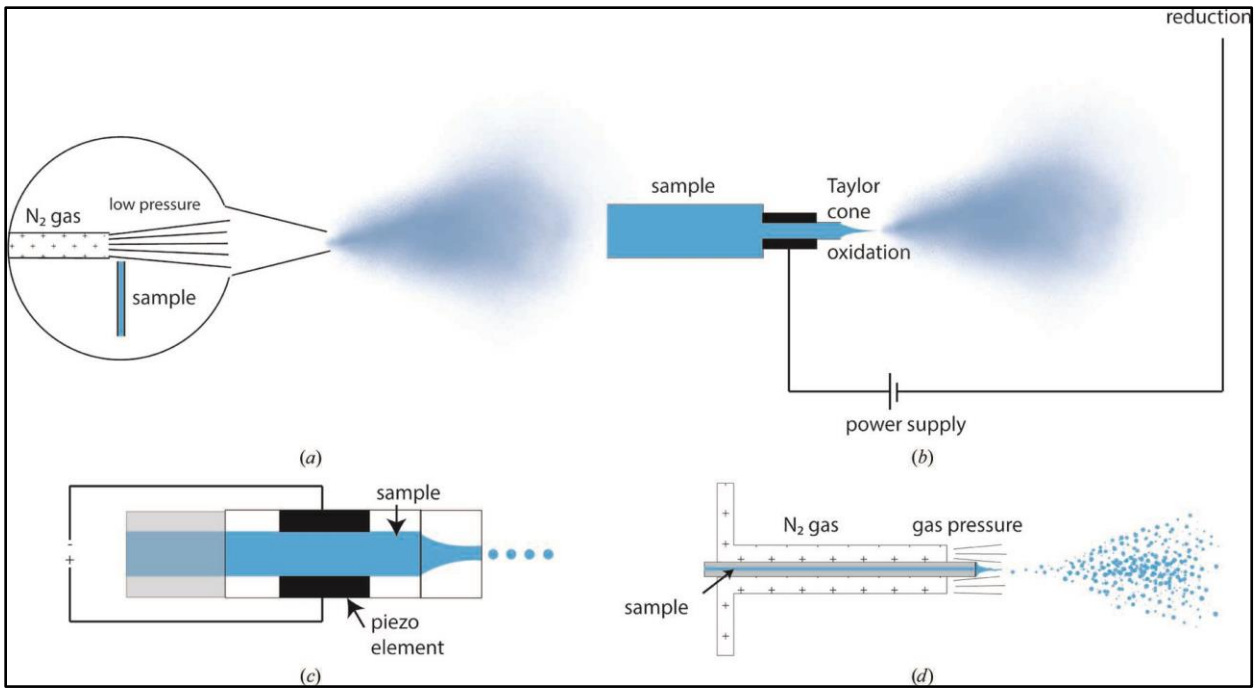

Figure 9. Sample dispensing methods for TRCEM. a) Atomizer spray based on Bernoulli's principle for generating very small droplets. b) Electrospray nozzle, which uses electric potential to ionize the sample and generate a fine mist of droplets. c) Piezoelectric nozzle, which generates droplets of uniform size using acoustic vibrations generated by the piezo element. d) Gas-assisted spray nozzle, which uses pressurized gas to break up the sample stream into small droplets and accelerate them toward the grid. From Maeots and Enchev, 2022 [23].

2.5 Challenges in TRCEM sample preparation

Despite significant developments in the method, there remain multiple challenges that limit the widespread application of TRCEM. The spraying method most commonly used for TRCEM sample preparation results in grids with far fewer collectible regions than the grids prepared by the conventional blotting method. The ice thickness is also quite variable resulting in low SNR in the data [91]. Both result in the requirement of more instrument time as well as

complicate downstream data processing. Drastic improvements in TRCEM sample preparation are necessary to produce higher-quality grids.

Another limitation of TRCEM is the requirement of large sample quantities. Current methods for TRCEM require 3-10 times [91] more samples than the conventional blotting method putting a huge strain on the biochemistry side of the process. New approaches shifting away from continuous flow methods have addressed these issues to some extent [92], but further work needs to be done.

Another limitation is the accuracy of reaction times for the experiments. Both on-grid and off-grid mixing approaches suffer from this issue. The reaction times attributed to an experiment do not reflect the real reaction times for the reactants. In the on-grid mixing approach, the interactions of the reactants with the air-water interface can affect the reaction whereas in the microfluidics-based approach, the velocity distribution under laminar flow causes a widening of the reaction time distribution [19, 20]. In contrast to on-grid mixing and reaction which are difficult to model, microfluidic-based TRCEM methods can be modeled quite well. Computational microfluidics models can be incorporated to better understand the kinetics underlying a biochemical reaction.

Chapter 3: PDMS-based microfluidics with internal SiO_2 coating for time-resolved cryo-EM

During my thesis work, I was involved in the development of PDMS-based microfluidic devices for TRCEM as well as modifying the time-resolved plunge freezing apparatus to interface with these microfluidic devices. This chapter outlines my contributions to the development of this PDMS-based TRCEM method.

3.1 Materials and Methods

3.1.1 Purification of *E. coli* 70S ribosomes

E. coli MRE600 cells were grown overnight at 37˚C in LB culture media to a final OD600 value of 0.81 units. The cells were harvested by centrifugation at 10,000 r.p.m. for 15 min at 4˚C. The cell pellet was washed with buffer containing 20 mM Tris-OAc (pH 7.5), 8 mM $Mg(OAc)_2$, 50 mM KCl, and 2 mM DTT. The cells were resuspended in the same buffer and lysed by ultrasonication. The lysate was centrifuged at 10,000 r.p.m. to remove cell debris and the supernatant was collected after passing through a filtering cloth. The filtered supernatant was diluted to a final volume of 300 ml using the lysis buffer and placed on top of a 30% sucrose cushion (in 20 mM Tris-oAC (pH 7.5), 8 mM $Mg(OAc)_2$, 500 mM KCl, and 2 mM DTT) and pelleted down using a Beckman Ti 45 rotor at 45,000 r.p.m. for 16 hr at 4˚C. The pellet was resuspended in a buffer containing 20 mM Tris-OAc (pH 7.5), 8 mM $Mg(OAc)_2$, 50 mM KCl, 2 mM DTT, and 10% sucrose. The resuspended pellet was treated with Puromycin at a final concentration of 1 mM at room temperature for 5 min before loading onto a 10% to 40% linear sucrose gradient in 20 mM Tris-OAc (pH 7.5), 8 mM $Mg(OAc)_2$, 50 mM KCl, and 2 mM DTT. The gradient was centrifuged using a Beckman SW 28 Ti rotor at 21,000 r.p.m. for 16 hr at 4˚C. Fractions were collected using Gilson FC2032B automated fraction collector. The 70S-containing fraction was collected and exchanged with 20 mM Tris-OAc (pH 7.5), 10 mM $Mg(OAc)_2$, 50 mM KCl, and 2 mM DTT buffer using dialysis. The ribosomes were concentrated, aliquoted, and flash-frozen using liquid nitrogen for storage.

3.1.2 Plunge freezing apparatus for TRCEM

The plunge-freezing apparatus used in our work is the same as described in [18] with some modifications. The apparatus does not contain the blotting and the high-tension modules. Additional gas lines for controlling the blotting and the cryogen shutter are also removed. A stage to hold the microfluidic devices is also added. The parameters specific to our apparatus are described in [93].

3.1.3 PDMS micromixer fabrication, SiO_2 coating and chip assembly

The protocol for the fabrication of the micromixer and sprayer for the PDMS microfluidic device, SiO_2 coating as well as the assembly of the chip is described in [93].

3.1.4 Testing adsorption of *E. coli* 70S ribosomes to the internal surface of the microfluidic device

To test the adsorption of the 70S to the chip surface, we passed 10 µl of 1.2 µM solution of 70S at a total flow rate of 6 µl/s through the chip. The flow-through was collected and its absorbance at 260 nm was measured using a NanoDrop® (Thermo Fisher Scientific, Waltham, MA, USA) spectrophotometer. The process was repeated for devices without any surface treatment, coated with n-dodecyl-β-D-maltoside (DDM), or coated with SiO_2. The SiO_2-coated devices were also tested for surface adsorption 1 day, 15 days, and 120 days after fabrication.

3.2 Results

3.2.1 PDMS-based modular microfluidics design

Our modular microfluidic design for TRCEM mixing-spraying devices is composed of three main parts: a PDMS-based SAR micro-mixer, a glass micro-capillary as a reaction channel, and a gas-assisted 3D micro-sprayer. The micro-mixer is capable of mixing two solutions with over 90% mixing efficiency within ~0.47 ms at a flow rate of 6 μL/s [93]. The micro-mixer is directly connected to a glass micro-capillary, which acts as the reaction channel. The dimensions of the capillary as well as the liquid flow rate determine the overall residence time within the channel. Different-sized capillaries can be connected to get different residence times. The glass capillary is connected to a gas-assisted 3D micro-sprayer. The overall design for the micro-sprayer is similar to the one described in [91] with a minor redesign to prevent dripping and allow operation at a lower gas pressure of 8 psi [93]. The modular design allows for the chip to be disassembled into its three components and for swapping out any parts necessary. The method to calculate the overall nominal reaction time for each time-resolved grid preparation experiment is described in [93].

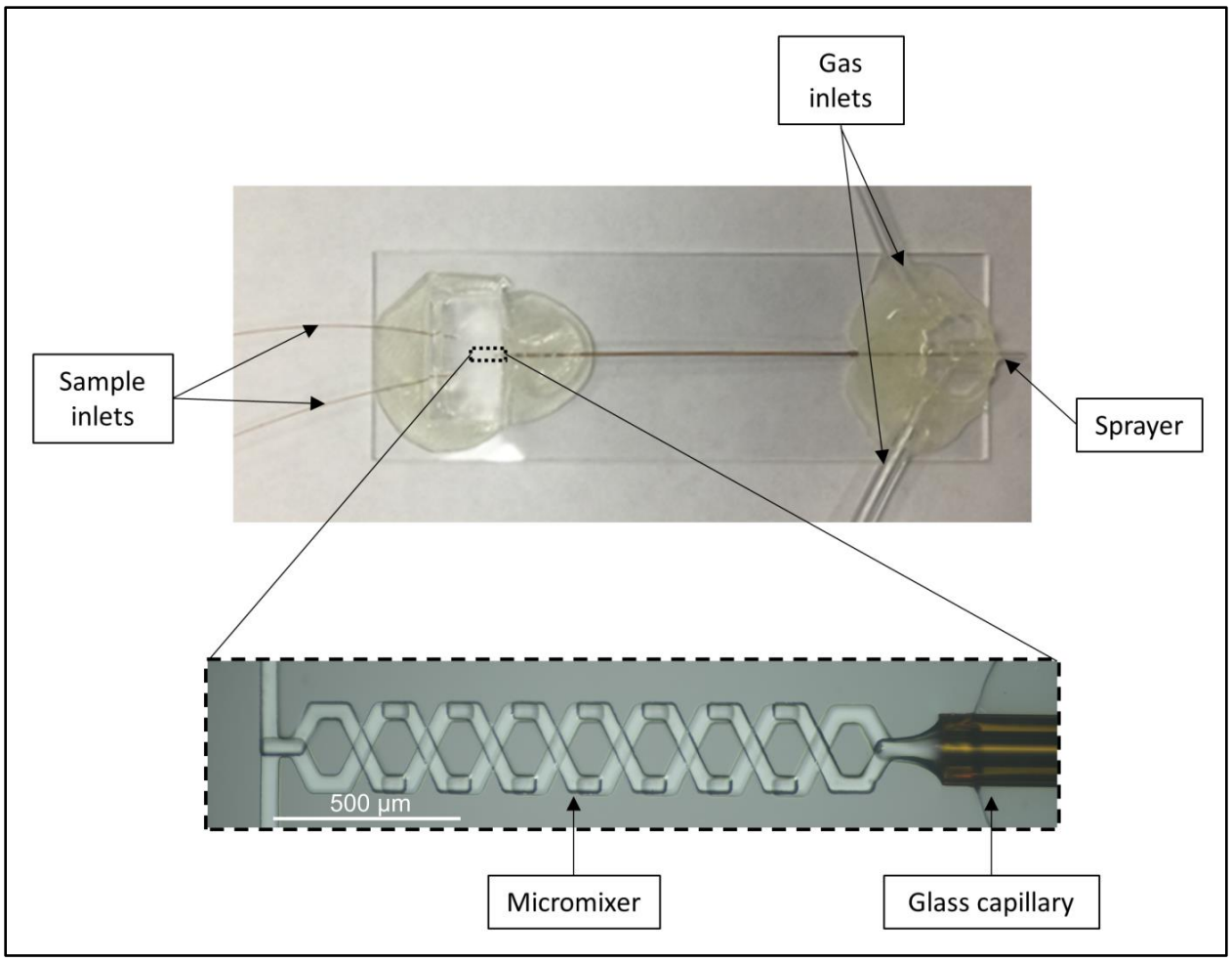

Figure 10. Modular microfluidic design for TRCEM with a PDMS-based SAR micro-mixer, a glass capillary for the reaction channel, and a gas-assisted 3D micro-sprayer.

3.2.2 SiO_2 surface coating to prevent sample adsorption

The internal surface of the PDMS micro-mixer was coated with a thin layer of SiO_2 using plasma-enhanced chemical vapor deposition (PECVD). The coating renders the internal surfaces hydrophilic [94] and acts as a barrier preventing samples from interacting with the PDMS surface. The sample adsorption to the chip surface after coating was tested as described in **Section 3.1.4**.

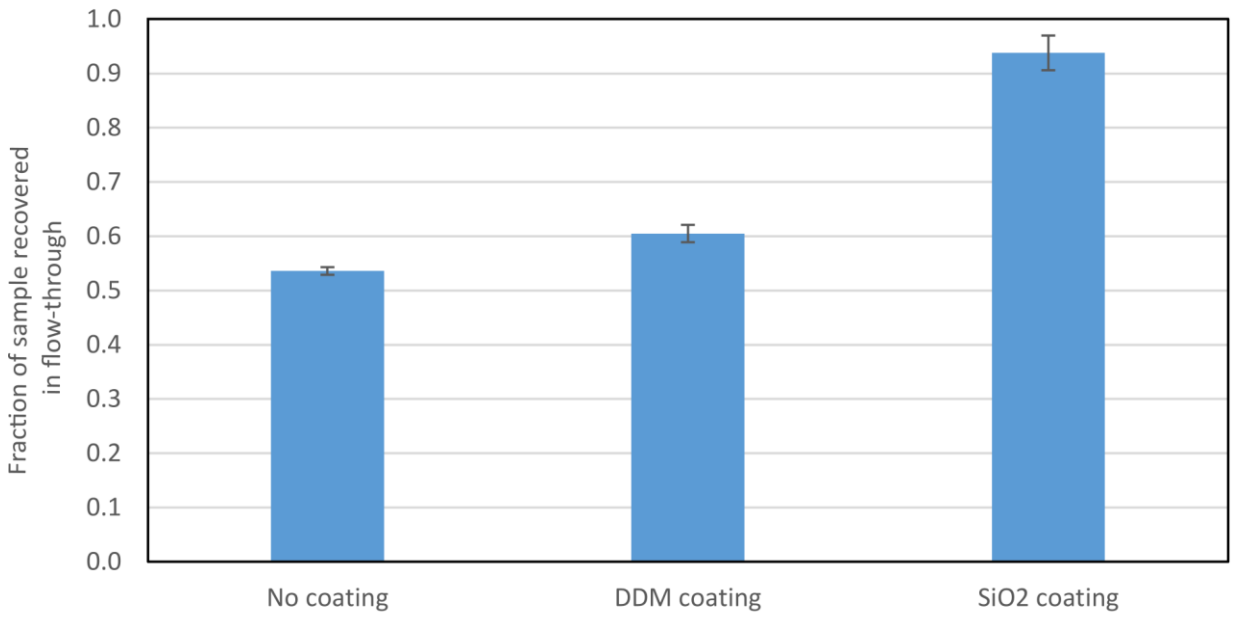

Figure 11. Sample adsorption to the PDMS chip surface with no coating, DDM coating, or SiO_2 coating.

Without any coating, the flow-through only retains ~54% of the input sample concentration. The flow-through concentration increases to ~60% after DDM surface treatment. The best results, however, were obtained with SiO_2 coating with a flow-through concentration of ~94% and the chip only adsorbing ~6% of the input sample concentration. We also assessed the stability of the SiO_2 treatment up to 120 days after coating. The flow-through experiments showed an increase in sample adsorption as more time passed after the SiO_2 coating process. On day 1, the flow-through had ~94% input sample concentration. The flow-through concentration dropped to ~85% of input on day 15 and further to 62% of the input on day 120 after coating. The SiO_2-coated chips performed better than the chips without coating even 120 days after the coating process. Based on these results, we decided to use the chips within one day of the coating process for the experiments described in **Chapter 4**.

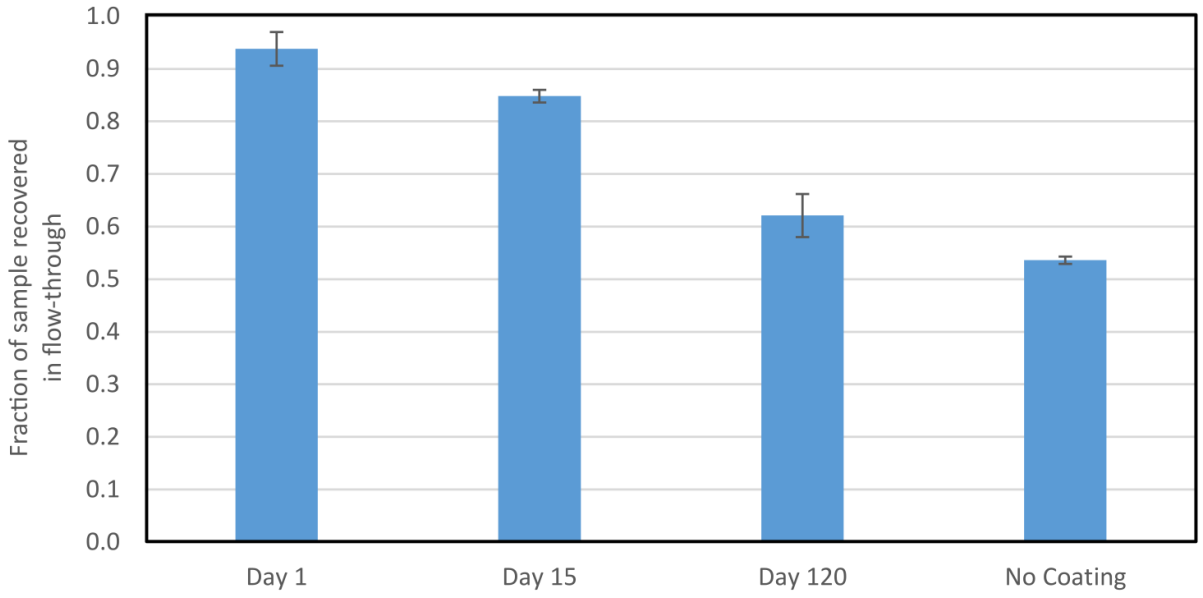

Figure 12. Sample adsorption results for SiO_2 coated chips day 1, day 15, and day 120 after coating as well as for chips with no coating.

Chapter 4: GTPase activation during mammalian translation termination captured using time-resolved cryo-EM

4.1 Introduction

Termination of translation is triggered when one of the three stop codons (UAA, UAG, or UGA) enters the ribosomal A site. In eukaryotes, the process is carried out by two RFs: eRF1 and eRF3. eRF1 is a tRNA-shaped protein that decodes the stop signal and catalyzes the hydrolysis of the peptide from the P-site tRNA. eRF3 is a GTPase that chaperones eRF1 and accelerates peptide release in a GTP hydrolysis-dependent manner. eRF1, eRF3, and GTP bind the pre-termination complex (pre-TC) as a ternary complex. The binding of the termination factors to the pre-TC induces compaction of the stop codon [2-6] causing it to adopt a UNR-type RNA U-turn conformation [95]. The compaction also brings the +4 position mRNA residue into the A site, stacking it with G626 of the 18S rRNA, which explains the preference for purines in the +4 position. The compacted state of the stop codon is stabilized by the GTS (31-33), E55, TASNIKS (58-64), and YxCxxxF (125-130) motifs in the NTD of eRF1. The +1 uridine is stabilized by hydrogen bonding with N61 and K63 of the TASNIKS motif, which would not be possible with cytidine in the same position. Additionally, the U-turn conformation of the stop codon excludes purines from the +1 position, making uracil the universal residue in the +1 position in eukaryotic stop codons. The +2 residue stacks onto the flipped-out switch base A1825, while A1824 remains within helix 44 of the 18S rRNA [5], and the +3 residue stacks onto the +2 residue. This stacking makes purines more preferable at the +2 and +3 positions. Additionally, the C127 of the YxCxxxF and E55 hydrogen bond with the +2 and +3 bases, which is only possible with purines in both positions. T32 of the GTS motif is positioned to hydrogen

bond with guanosine at the +3 position, but only when the +2 residue is adenosine (UAA or UAG). When the +2 residue is a guanosine (UGA or UGG), the GTS loop gets displaced away from the stop codon by ~4Å causing T32 to face away from the +3 position and unable to hydrogen bond. The UGG codon, which codes for tryptophan, is further discriminated from the stop codons by the hydrogen bonding requirement of E55 as well as the repulsion between their O6 atoms upon stacking [5]. Perturbation in any of the eRF1 motifs mentioned affects the stop codon recognition efficiency and specificity [96-98]. After stop codon recognition by eRF1, eRF3 hydrolyzes the GTP and eventually dissociates. eRF1's M domain undergoes a 140° rotation relative to the NTD, adopting an extended conformation. α-helix 8 in the M domain and α-helix 9 in the CTD, which were separated by an eRF3-induced kink in the ternary complex, relax to form a continuous α-helix. This places the catalytic GGQ motif at the tip of the M domain in the PTC, where it catalyzes the release of the nascent peptide chain and forms the post-termination complex (post-TC), preparing the ribosome for recycling [1-12]. The structures for the ternary complex-bound pre-TC trapped using non-hydrolysable GTP analogs as well as for the post-TC have been captured by cryo-EM [3, 4, 11, 12]. The cryo-EM structures revealed the interactions between the RFs and the pre-TC in atomic detail. Recent single-molecule fluorescence microscopy experiments also revealed the time scales for the translation termination events in yeast. The factors bind to the pre-TC quickly (<1 s) followed by stop codon decoding, GTP hydrolysis, and eRF3 dissociation (~0.5 s). eRF1 accommodation and peptide release occurs slowly (~3 s) after which eRF1 quickly dissociates from the ribosome (~ 0.5 s) [10]. Despite previous efforts, the structural and conformational dynamics of ribosomes and RFs necessary for RF activation during eukaryotic translation termination remain poorly understood. In this work, we address this gap in knowledge by capturing structures of intermediates formed

during eukaryotic translation termination using TRCEM. We use the reaction between an in vitro-reconstituted pre-TC mimic and the ternary complex of recombinant RFs with GTP to capture the structures of intermediates formed during the termination process. We assembled the pre-TC mimic using a type IV IRES from the intergenic region of HalV with the first sense codon mutated to a UAA stop codon (Figure 12a). The HalV IRES can bind to 80S ribosomes directly without the requirement of any initiation factors and position the first sense codon in the ribosomal A site. The HalV IRES-STOP construct was observed to bind eRF1•eRF3, as shown by toe-printing analysis [47]. Our long-time-scale (10 min) cryo-EM experiments also revealed that the construct can accommodate eRF1 into the PTC post-eRF3 release. We performed TRCEM experiments using the mixing-spraying method for reaction times of 450 ms and 900 ms, as well as the on-grid mixing and blotting method for reaction time of 15 s. Data analysis yielded structures of four intermediates formed during the termination process with $FSC_{0.143}$ resolution between 3.3 Å and 4.1 Å. The structures reveal the mechanism for GTPase activation as well as a potential mechanism for GDP release post-GTP-hydrolysis.

4.2 Materials and Methods

4.2.1 Expression and purification of proteins and ribosomes

Native mammalian 40S and 60S subunits were purified from rabbit reticulocyte lysate (RRL) as described in [2]. The HalV IRES-STOP mRNA was transcribed as described in [47]. Recombinant eRF1 and N-terminal truncated eRF3 (aa 139-499) were expressed and purified from *E. coli* as described [2].

4.2.2 Chip fabrication

The PDMS-based microfluidic chips were fabricated as described in **Chapter 3**. The parameters specific to this work are in **Table 1**.

Microfluidic Chips	Capillary tubing (as microreactor) inner diameter (I.D.) and length (μm/mm)	Tubing (between micromixer and microreactor) I.D. and length (μm/mm)	Tubing (between microreactor and sprayer) I.D. and length (μm/mm)	Sprayer -grid distance (mm)	Sprayer-cryogen distance (mm)	Plunging velocity (m/s)
Chip 1 (455 ms)	200/84.0	75/2.6	75/5.9	3.5	15	1.9
Chip 2 (898 ms)	300/75.0	75/2.5	75/5.5	3.5	15	1.9

Table 1. Parameters for chip fabrication and TRCEM sample preparation. The times mentioned are the overall reaction times between mixing and freezing. (Reaction times are rounded to 450 ms and 900 ms in further discussion for simplicity)

4.2.3 Assembly of pre-TC and ternary complex

The pre-TC was assembled by mixing rabbit 40S subunit, 60S subunit, and HalV IRES-STOP mRNA in Tris buffer (20 mM Tris at pH 7.5, 100 mM KCl, 2mM DTT, 2.5mM $MgCl_2$, 0.5 mM spermidine) at final concentrations of 3.5 μM, 3.5 μM, and 8 μM, respectively. The termination ternary complex was assembled by mixing eRF1, eRF3, and GTP in Tris buffer (20 mM Tris at pH 7.5, 100 mM KCl, 2mM DTT, 2.5mM $MgCl_2$, 0.5 mM spermidine) at final concentrations of 10 μM, 10 μM, and 1 mM, respectively. Both mixtures were incubated separately at 37 ˚C for 10 min before grid preparation.

4.2.4 Preparation of grids using the mixing-spraying method

The grids corresponding to 450 ms and 900 ms reaction times were prepared using the TRCEM mixing-spraying method described in **Chapter 3**. Quantifoil R0.6/1 holey carbon grids with 300 Cu mesh were glow discharged for 40 s in air plasma at 15 mA and 0.26 mBar using a PELCO easiGlow glow discharge unit. The pre-TC and the ternary complex were aspirated into two separate syringes on the plunge freezing apparatus at the concentrations mentioned in **Section 4.2.3**. The syringes were connected to a PDMS-based microfluidic mixing-spraying device. The device was placed inside an environmental chamber kept at room temperature with a relative humidity of 90-95%. Devices with different reaction channel lengths were used for the two different reaction times (Table 1). The two reactants were injected into the mixing-spraying device at flow rates of 3 **μ**L/s each (6 **μ**L/s total flow rate). After mixing and reacting inside the microfluidic device, the solution was sprayed using humidified N_2 gas at 8 psi gas pressure. A cryo-EM grid was passed through the spray and plunged into liquid ethane for vitrification. The grids were transferred to a grid storage box and stored under liquid nitrogen.

4.2.5 Preparation of grids using the blotting method

The grids for the 15 s and 10 min reactions were prepared via the blotting method. Grids were glow discharged as mentioned in **Section 4.2.4**. Grids were prepared using a Vitrobot Mark IV (Thermo Fisher Scientific, Waltham, MA) at room temperature with 100% relative humidity. The reactants were diluted 3.5 times before application to the grid. For the 15 s reaction time, the reaction was performed on the grid. 2 **µ**L of ternary complex was first applied to the grid followed by the application of 2 **µ**L of the pre-TC complex. The two were mixed on the grid by agitation via pipetting. For the 10 min reaction time, the reaction was performed by mixing and incubating the two reactants in a test tube at room temperature. 3 **µ**L of the mixture was then applied to the grid. After application, the sample was blotted with blot force 3 for 4 s in both cases and plunged into liquid ethane for vitrification. The overall time between sample application and plunge freezing for the 15 s reaction time was measured using a stopwatch. The grids were transferred to a grid storage box and stored under liquid nitrogen.

4.2.6 Cryo-EM data collection

Data for the 450 ms, 900 ms, and 15 s reaction times were collected using a 300 kV Titan Krios transmission electron microscope (Thermo Fisher Scientific) equipped with a Gatan K3 direct electron detector (Gatan, Inc., Pleasanton, CA) and a post-column GIF quantum energy filter. Movies were collected in counting mode within a defocus range of -1.0 to -2.5 **µ**m at a nominal magnification of 105,000× resulting in a raw pixel size of 0.83 Å/pixel. Leginon [100] was used for semi-automated target selection and movie acquisition. A 30° stage tilt was employed during data collection to compensate for the preferred orientation observed in the data. Each movie is composed of 50 frames collected over a 2.5 s exposure with a dose rate of ~16 e^-

/pixel/s resulting in a total dose of ~58 $e^-/Å^2$. Data for 10 min reaction time were collected using a 300 kV Tecnai Polara F30 (Thermo Fisher Scientific) equipped with a Gatan K3 direct electron detector (Gatan, Inc.). Movies were collected in counting mode within a defocus range of -0.5 to -3.5 **µ**m at a nominal magnification of 52,000× resulting in a raw pixel size of 0.95 Å/pixel. Leginon was used for semi-automated target selection and movie acquisition. 40% of the movies were collected with a 30° stage tilt to compensate for the preferred orientation observed in the data. Each movie is composed of 40 frames and collected over a 4 s exposure with a dose rate of ~16 e-/pixel/s resulting in a total dose of ~71 $e-/Å^2$.

4.2.7 Image processing

The movies were visually inspected for quality. 7,319, 13,405, 10,245, and 20,151 good movies were selected for downstream processing from the 450 ms, 900 ms, 15 s, and 10 min datasets, respectively. Data were primarily processed using Relion 3.1 [101-103]. Movies were corrected for beam-induced motion and dose-weighted average images were produced using Relion's implementation of the MotionCor2 [104] algorithm. The contrast transfer function (CTF) was estimated using GCTF [105]. Particle picking was performed using crYOLO 1.8.4 [106] neural network-based picker. Particles were initially manually picked from a small subset of ~1000 images and used for training the neural network. The trained neural network was then used to pick particles for the entire dataset. The picked particles were extracted with a box size of 492 pixels for the 450 ms, 900 ms, and 15 s datasets and 480 pixels for the 10 min datasets, respectively. Particle images from the 450 ms, 900 ms, and 15 s datasets were combined for downstream processing. Particle images from the 10 min dataset were processed separately.

The combined particle images from the 450 ms, 900 ms, and 15 s datasets were subjected to multiple rounds of 2D classification in Relion 3.1. Around 310k particle images belonging to 80S-like 2D classes were manually selected for downstream processing. A starting 3D model was generated using Relion's 3D initial-model module. This starting model was then used as a reference in Relion's 3D auto-refine module to estimate the relative orientations and translations of the particle images and to generate a consensus 3D map. The particles were then subjected to 3D classification without additional image alignment, resulting in four different classes: Class 1 with 200k particles had the ribosome with a non-rotated SSU, Class 2 with 43k particles had the ribosome with a rotated SSU, Class 3 with 41k particles had the ribosome with SSU head-swivel and Class 4 with 26k particles had the ribosome at low resolution. Classes 2 and 3 were rejected due to being intermediates for IRES-mediated assembly of pre-TC, and Class 4 was rejected due to its low resolution. Class 1 with non-rotated ribosome was selected for downstream processing. The selected particles were subjected to another round of 3D auto-refinement. Per-particle CTF parameters were optimized using Relion's CTF refinement module. The particles were then subjected to Bayesian polishing [107] to correct for residual motion left over after initial motion correction. The polished particles were re-extracted after binning to 1.34 Å/pixel with a box size of 304 pixels and subjected to 2D classification. 195k particles with good 2D class averages were selected for subsequent 3D auto-refinement and CTF refinement. This resulted in a consensus map with a non-rotated ribosome at $FSC_{0.143}$ resolution of 2.9 Å (masked). For separating the different RF conformations, we used masked classification with signal subtraction. Atomic models for pre-TC (PDB: 5LZT) and post-TC (PDB: 5LZU) were rigid-body fitted into the consensus map using Chimera [108]. Chains corresponding to RFs in both models were selected and molmap command was used to generate a hybrid density map with a Gaussian width of 8 Å.

The resulting map was used to generate a mask using Relion's mask creation module with a soft edge of 6 pixels. The mask covered the binding region for eRF3 as well as for eRF1 in both pre-accommodation and post-accommodation states. Two additional masks were generated in the same manner for the RFs from the pre-TC and post-TC models separately. Signal subtraction with the hybrid mask was performed using Relion's signal subtraction module to remove the signal outside the masked region. The subtracted images were used for the classification of RF states using Relion's 3D classification module (**Figure 10**). The classification resulted in six classes: Class 1 with 94k particles had an RF-free ribosome, Class 2 with 35k particles had a ribosome with a PTC accommodated eRF1, Class 3, 4, and 5 with 26k, 11.7k, and 7.4k particles had ribosomes with both RFs bound in different conformations, and Class 6 with 20.7k had ribosome with both RFs bound but the density for eRF3 G-domain was missing. After classification, we reverted to the non-subtracted images for 3D auto-refinement of individual classes. Multiple iterations of 3D refinement and CTF refinements were performed resulting in final maps with $FSC_{0.143}$ resolutions ranging from 3.0 Å to 4.2 Å (**Table 2**).

The particle images for the 10 min dataset were binned 8 times and subjected to multiple rounds of 2D classification in Relion 3.1. 680k particles with good 2D class averages were selected for further processing. The particles were re-extracted with 4 times binning and subjected to 3D auto-refinement followed by 3D classification. Classification yielded three classes: Class 1 with 507k particles had the ribosome with a non-rotated SSU, Class 2 with 86k particles had the ribosome with a rotated SSU, and Class 3 with 87k particles had the LSU with missing SSU density. Class 1 with visible eRF1 density was selected for downstream processing. Particle images were un-binned and duplicate particles were removed using a 250 Å distance cutoff resulting in 496k particles. The particles were subjected to 3D refinement and CTF

refinement in Relion 3.1 resulting in a map with an $FSC_{0.143}$ resolution of 2.9 Å. Focused 3D classification was performed using the hybrid mask mentioned earlier. The classification yielded two classes: Class 1 with 381k particles had a ribosome with an accommodated eRF1, and Class 2 with 115k particles had a ribosome with an empty A site. No eRF3 bound classes were observed. Class 1 was selected and subjected to multiple rounds of 3D refinement and CTF refinement resulting in a final map with $FSC_{0.143}$ resolution of 2.95 Å (**Figure 11**).

Local B-factor estimation and sharpening were performed using PHENIX's [109] auto-sharpen module and resulting maps were up-sampled 2 times in COOT [110] before atomic model building and refinement.

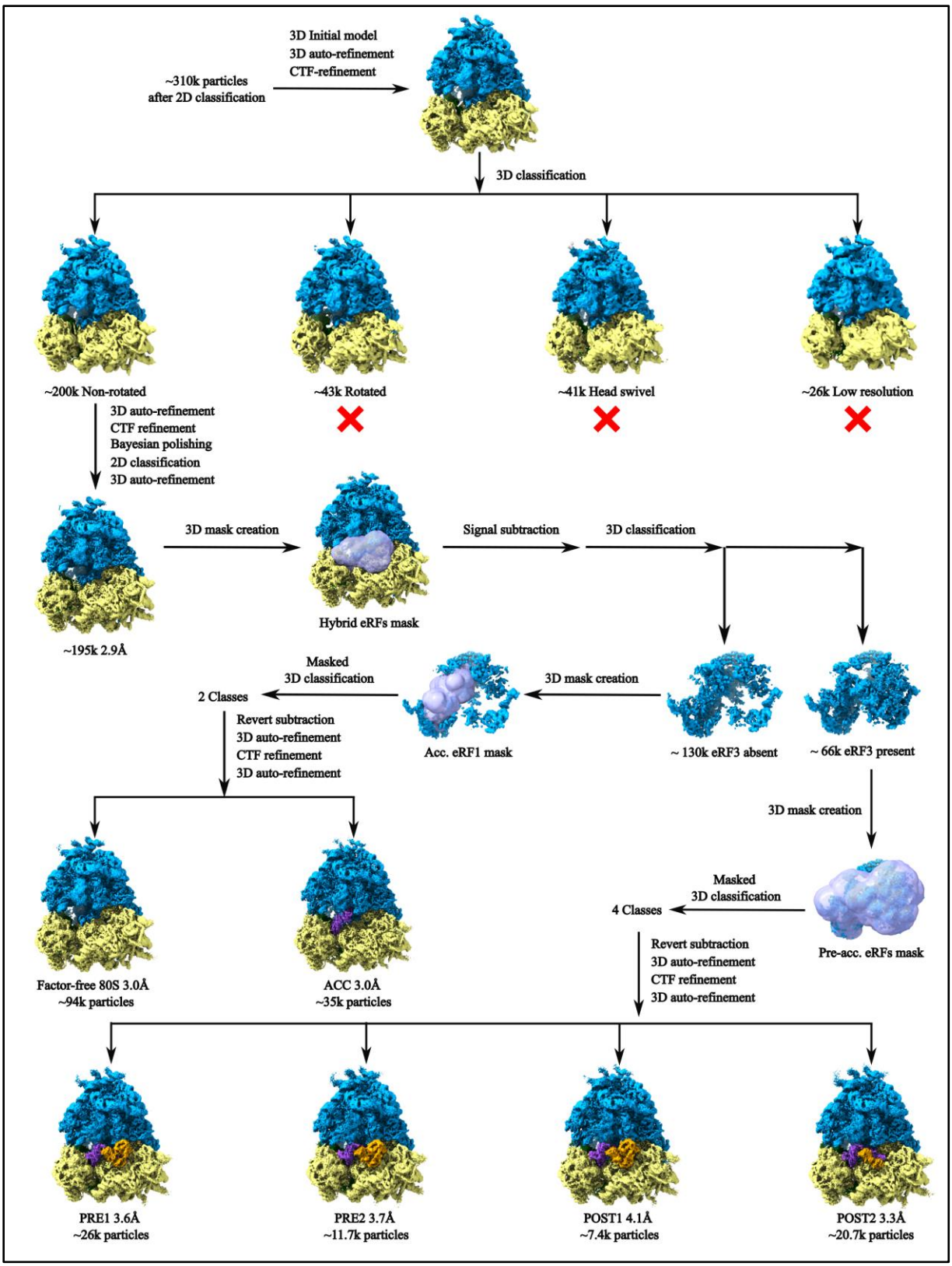

Figure 13. Classification regime for the combined 450 ms, 900 ms, and 15 s datasets.

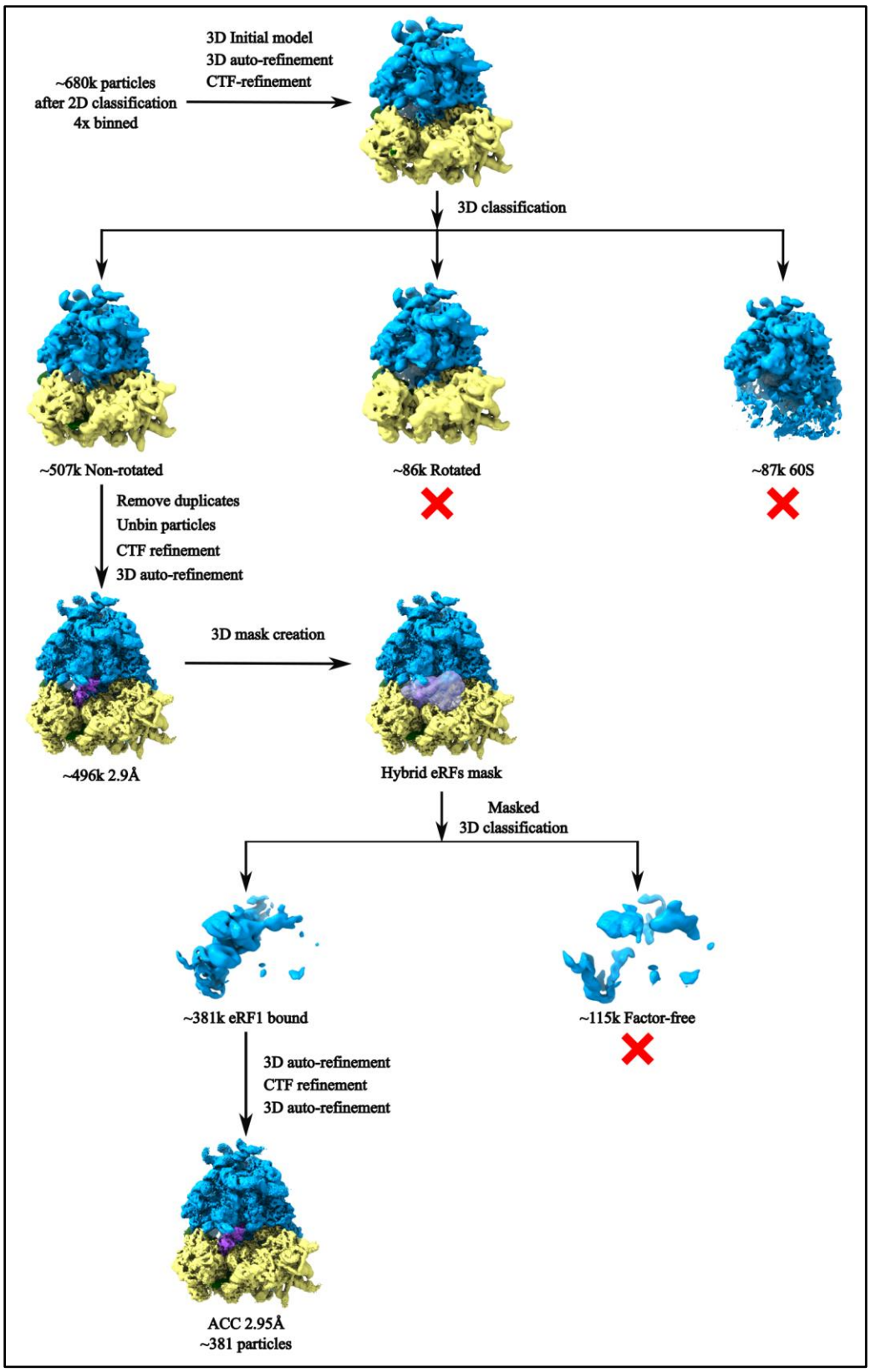

Figure 14. Classification regime for the 10 min dataset.

4.2.8 Atomic model building and refinement

Atomic models for the rabbit ribosome and the HalV IRES from PDBs 7O7Y and 6ZVK, respectively, were docked into the sharpened maps using ChimeraX [111]. Models were manually adjusted and the STOP codon was modeled in COOT. Atomic coordinates were refined against the maps using PHENIX real-space refinement with secondary structural restraints. Pre-accommodated RFs or post-accommodated eRF1 from PDB: 5LZT or 5LZU, respectively were docked into the maps using ChimeraX and manually adjusted in COOT. GTP or GDP from PDB: 1WDT or 7ST7, respectively, were similarly docked and adjusted. The models were combined and subjected to real-space refinement in PHENIX. Models were validated using Phenix's comprehensive validation tool (Table 2) [113, 114].

Map					
Class	**PRE1**	**PRE2**	**POST1**	**POST2**	**ACC**
Particles	26046	11784	7449	20712	34873
Map resolution at $FSC_{0.143}$ (Å)	3.6	3.7	4.1	3.3	3.0
Map sharpening B-factor ($Å^2$)	-57	-46	-48	-52	-44
Refinement					
Model composition (residues)					
Proteins	12429	12429	12419	12204	11995
Nucleotides	5479	5478	5480	5478	5478
GDP	0	0	1	0	0
GTP	1	1	0	0	0
Zn	8	8	8	8	8

SPD	25	28	25	28	25
SPM	3	3	2	3	3
Mg^{2+} ions	261	267	265	268	273
Average B factors ($Å^2$)					
Proteins	90.94	96.36	106.12	95.73	81.62
Nucleotides	81.92	95.16	99.24	103.17	90.06
Ligands	61.34	70.79	74.73	72.29	68.19
R.m.s. deviations					
Bonds (Å)	0.003	0.003	0.003	0.003	0.003
Angles (degree)	0.549	0.538	0.555	0.572	0.598
Validation					
Molprobity score	1.09	1.04	1.15	1.1	0.98
Clash score	2.47	2.57	2.9	2.8	2.07
Rotamer outliers (%)	0.01	0.00	0.00	0.00	0.00
Ramachandran plot					
Outliers (%)	0.00	0.00	0.00	0.00	0.00
Allowed (%)	2.27	1.96	2.34	2.15	1.88
Favored (%)	97.73	98.04	97.66	97.85	98.12

Table 2. Model refinement and validation statistics.

4.3 Results

4.3.1 TRCEM reveals five factor-bound classes

We decided to use a duration of 450 ms for our initial time-resolved experiments. We based this choice on the termination time scales that were observed in yeast using single-molecule fluorescence experiments [10]. After analyzing the initial data, we selected two additional reaction time points of 900 ms and 15 s. By processing the data from all three reaction times together, we were able to identify four intermediates that ranged in resolution from 3.3 to 4.2 Å at $FSC_{0.143}$. We also discovered a class with eRF1 that was accommodated into the PTC, matching the one observed in the 10 min control experiment (**Figure 12c**). All four intermediate classes had a non-rotated 80S ribosome with pre-accommodated eRF1 and eRF3 that were bound in various conformations. Through population analysis (**Figure 12b**) and atomic model building, we were able to assign a chronological order to the intermediates and determine the hydrolysis state of the eRF3-bound GTP. Classes 1 and 2 represented pre-hydrolysis states that contained intact GTP, and so we named them PRE1 and PRE2. Class 3 represented a post-hydrolysis and post-Pi-release state that contained GDP and was named POST1. Class 4 represented a state with a disordered eRF3 G-domain, suggesting it to be a post-GDP release state, and therefore we named it POST2. The post-accommodated eRF1 state was named ACC.

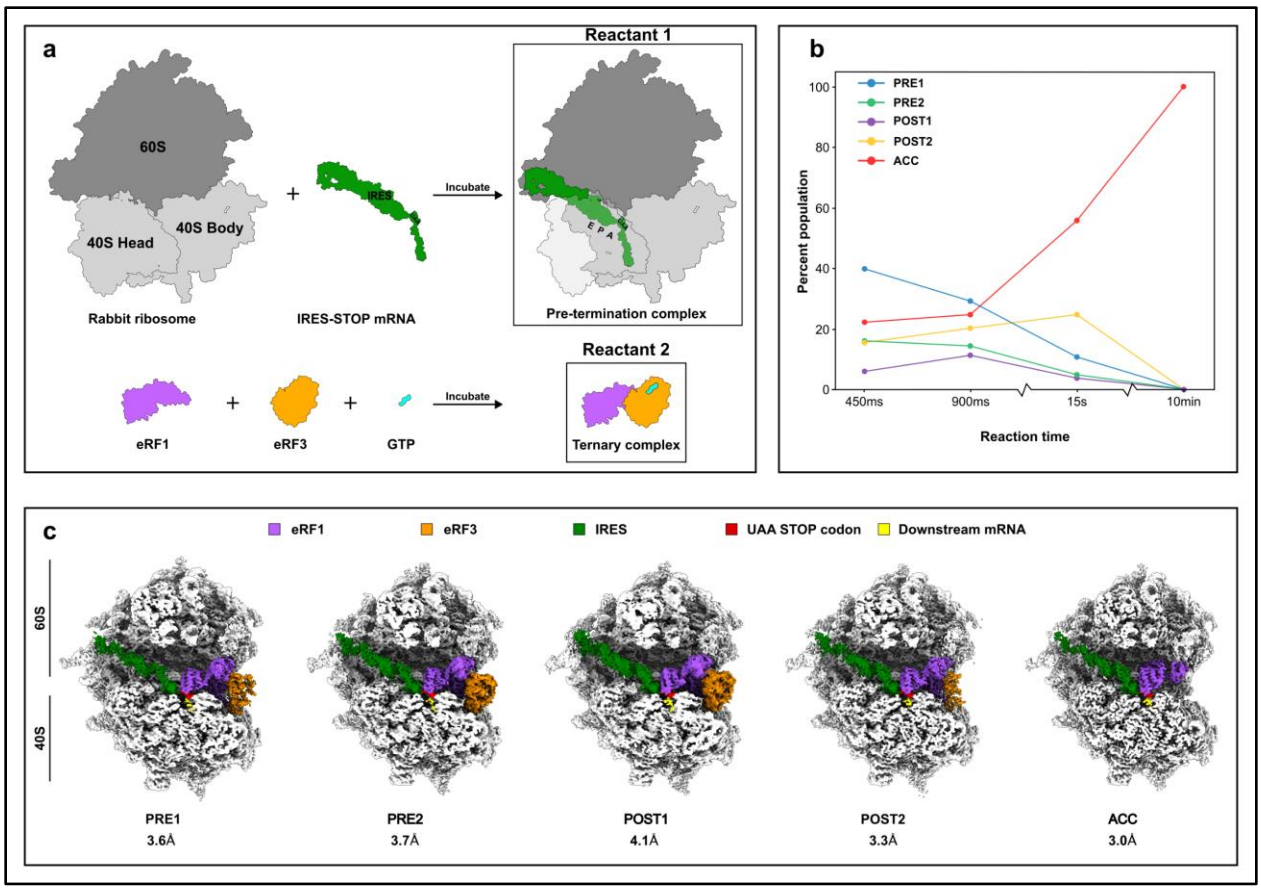

Figure 15. Reactants used and overall results for the translation termination TRCEM experiments. a) Assembly of the pre-TC and the termination ternary complex. b) Distribution of relative populations of the factor-bound classes at the different reaction times. c) Sliced views of the density maps for the factor-bound classes ordered chronologically from left to right. The maps show the 80S inter-subunit space with densities for the IRES-STOP mRNA and the RFs.

4.3.2 Limitations in the accuracy of reaction times

Although we have assigned specific reaction times to the different datasets, these are only nominal reaction times determined either analytically (for the 450 ms and 900 ms datasets) or empirically using a stopwatch (for the 15 s and 10 min datasets). The accuracy of these reaction times depends on a few assumptions, not all of which are true for each sample preparation method used. The first important assumption is that the two reactants are mixed efficiently within a small proportion (ideally <10%) of the overall reaction time. For the 450 ms and the 900 ms, this assumption is true as the mixing takes place in PDMS-based microfluidic devices described in **Chapter 3** resulting in an overall mixing efficiency of >90% with a mixing time of ~0.47 ms at a flow rate of 6 μL/s [93]. For the 15 s and 10 min reaction times, the mixing primarily takes place by agitation by pipetting followed by diffusion. Although the mixing efficiency in this case cannot be accurately determined due to the stochastic nature of pipette-assisted mixing, a comparison of the factor-bound population fractions of the non-rotated pre-TC clearly shows that the mixing is inadequate at least for the 15 s experiment (**Figure 16**). The factor-bound fraction of the non-rotated pre-TC is expected to increase as we increase the reaction time. The trend followed by the 450 ms, 900 ms, and 10 min experiments, but not the 15 s experiment. The low proportion of factor-bound pre-TC in the 15 s experiments suggests that the reactants are likely not mixed well and the reaction rate is diffusion-limited.

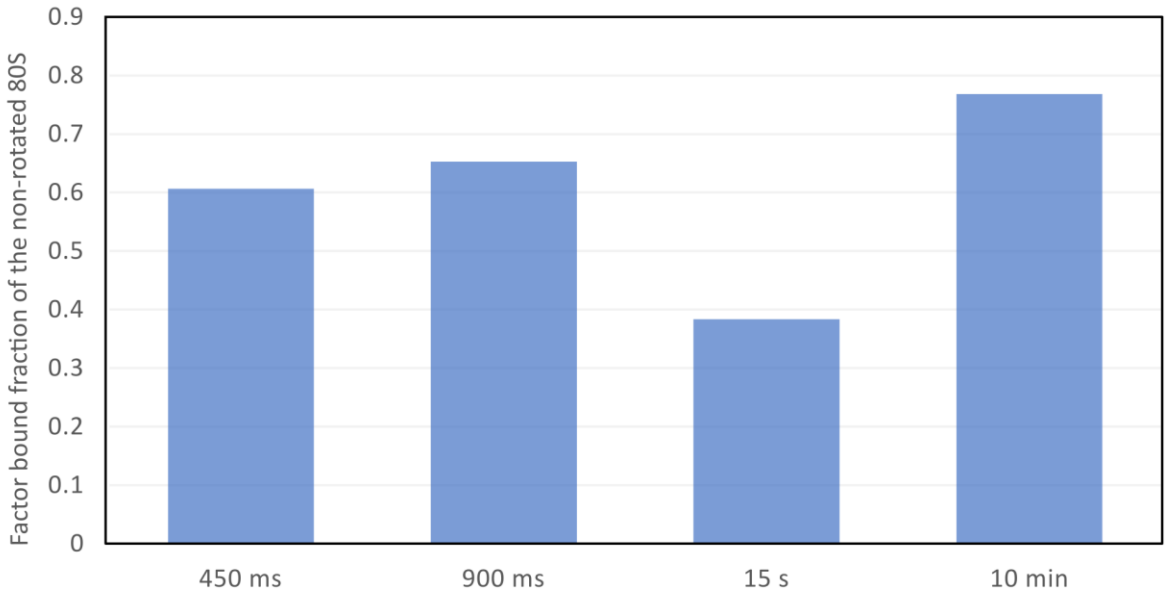

Figure 16. Fraction of non-rotated 80S bound by the termination factors for experiments with nominal reaction times of 450 ms, 900 ms, 15 s, and 10 min, respectively.

The second major assumption is the reaction takes place under the same conditions for the same amount of time throughout the volume of the mixture before freezing. For the 450 ms and 900 ms experiments, the bulk of the reaction takes place in continuous laminar flow inside a glass capillary. Under laminar conditions, the velocity of fluid flow inside a cylindrical channel varies radially, with the fluid closer to the channel walls moving slower than the fluid toward the center of the channel. The residence time distribution E(t) for such laminar flow is given by equation (1) [112]

$$E(t) = \begin{cases} 0 & , \quad t < \tau/2 \\ \dfrac{\tau^2}{2t^3} & , \quad t \geq \tau/2 \end{cases} \qquad (1)$$

where τ is the mean residence time, given by the volume of the tube divided by the volumetric flow rate. The residence time distributions for mean residence times of 450 ms and 900 ms are plotted in **Figure 17.** We have neglected the times associated with mixing, spraying, plunging, and freezing for simplicity. The figure shows that the residence times are non-uniform with 50% of the sample volume spending between τ/2 to τ time inside the channel. It also shows that the distribution gets wider as τ increases.

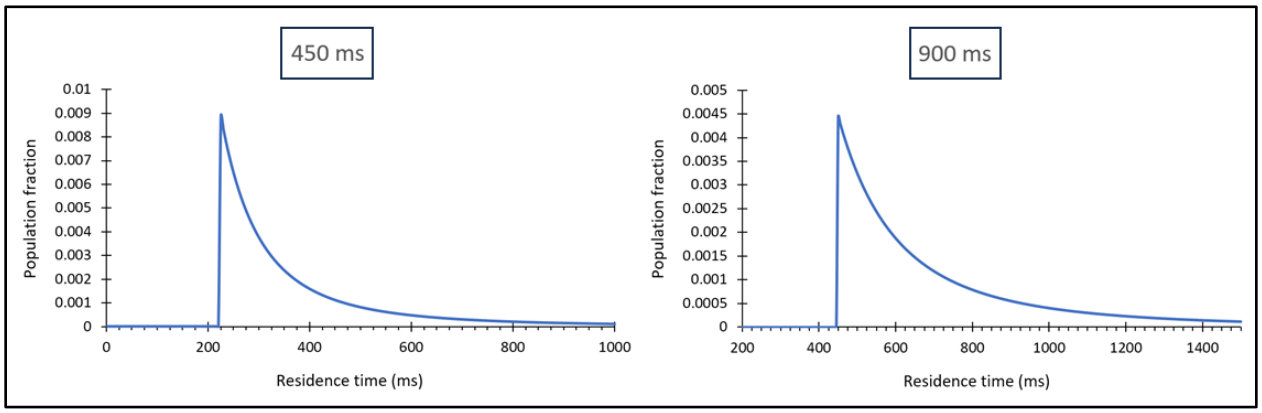

Figure 17. Residence time distributions for laminar flow in a cylindrical channel with mean residence times of 450 ms (left) and 900 ms (right).

For the 15 s and 10 min experiments, the bulk reaction takes place in static fluid, so the dispersion of residence time is not an issue. The reaction for the 15 s experiment primarily takes place on the surface of the grid, which exposes the reaction mixture to the air-water interface. This could potentially alter the reaction conditions and affect the reaction kinetics as discussed in **Section 2.4.2**. Taken together, all these facts suggest that nominal residence times assigned to these experiments are an approximation and do not reflect the exact reaction times experienced

by all the molecules of the sample. Therefore, precautions should be taken when using these results for obtaining reaction kinetics.

4.3.3 eRF1 conformations during termination

N-terminal domain

The eRF1 NTD reaches into the ribosomal A site and forms multiple interactions with the ribosome, mRNA, and the anti-codon mimicking pseudoknot PKI of the IRES. The interactions between eRF1's NTD and the stop codon are already formed in the earliest state observed and remain unchanged throughout the termination process. The interactions are similar to the ones observed in previous structures [3, 4, 11, 12]. The stop codon adopts a compacted conformation with the A (+3) stacking with A (+2). The A (+2) nucleotide coordinates a magnesium ion and stacks with the flipped-out switch base A1825, while the A1824 switch base remains within the helix 44 of the 18S rRNA. The A (+4) nucleotide downstream of the stop codon stacks with G626 of the 18S rRNA. eRF1 interacts with the stop codon using multiple residues of the conserved $TASNIKS_{58\text{-}64}$, $YxCxxxF_{125\text{-}131}$ and $GTS_{31\text{-}33}$ motifs as described in **Section 1.7.2**. Three residues of the TASNIKS motif (N61, I62, and K63) hydrogen bond with U (+1) of the stop codon. N61 side chain hydrogen bonds with O2 of U(+1), K63 side chain hydrogen bonds with O4 of U(+1), and the backbone carbonyl of I62 hydrogen bonds with the N4 of U (+1). Additionally, the side chain of T58 hydrogen bonds with N6 of A(+3). C127 of the YxCxxxF motif hydrogen bonds with N6 of A(+2) using its side chain. Lastly, T32 of the GTS motif hydrogen bonds with N3 of A(+3) using its side chain. E55 side-chain implicated in discriminating UGG codon (codes for tryptophan) from the stop codons [3] is not visible in our

maps (**Figure 13**). The interactions anchor the loop joining α2 and α3 helices in position, preventing dissociation of the RFs and allowing for sampling of states necessary for successful accommodation.

On the opposite side of the α2 and α3 helices, eRF1 loop regions form multiple interactions with the helix 69 of the LSU (**Figure 14**). The interactions primarily occur via side-chain hydrogen bonds between eRF1 loop regions N121-S123 and K42-R47 and the phosphate backbone of helix 69. The interactions are fewer and weaker in PRE1 but become closer and stronger for subsequent classes as eRF1 moves further into the A site. The NTD also interacts with R130 of the SSU ribosomal protein uS19. The interaction is only visible in PRE1, PRE2, and POST2 and becomes unclear/disappears in POST1 and ACC. Lastly, NTD interacts with PK1 of the IRES. The interactions only appear in POST1 and ACC states where the eRF1 NTD helix α2 docks against PKI. The interactions occur mainly via backbone hydrogen bonding, with K50 being the only eRF1 side chain to interact directly with PK1. The increasing interactions with the ribosome and the PKI likely drive the encroachment of eRF1 further into the A site. This encroachment also pulls eRF3 closer to the ribosome and facilitates its anchoring to the SSU and subsequent GTPase activation.

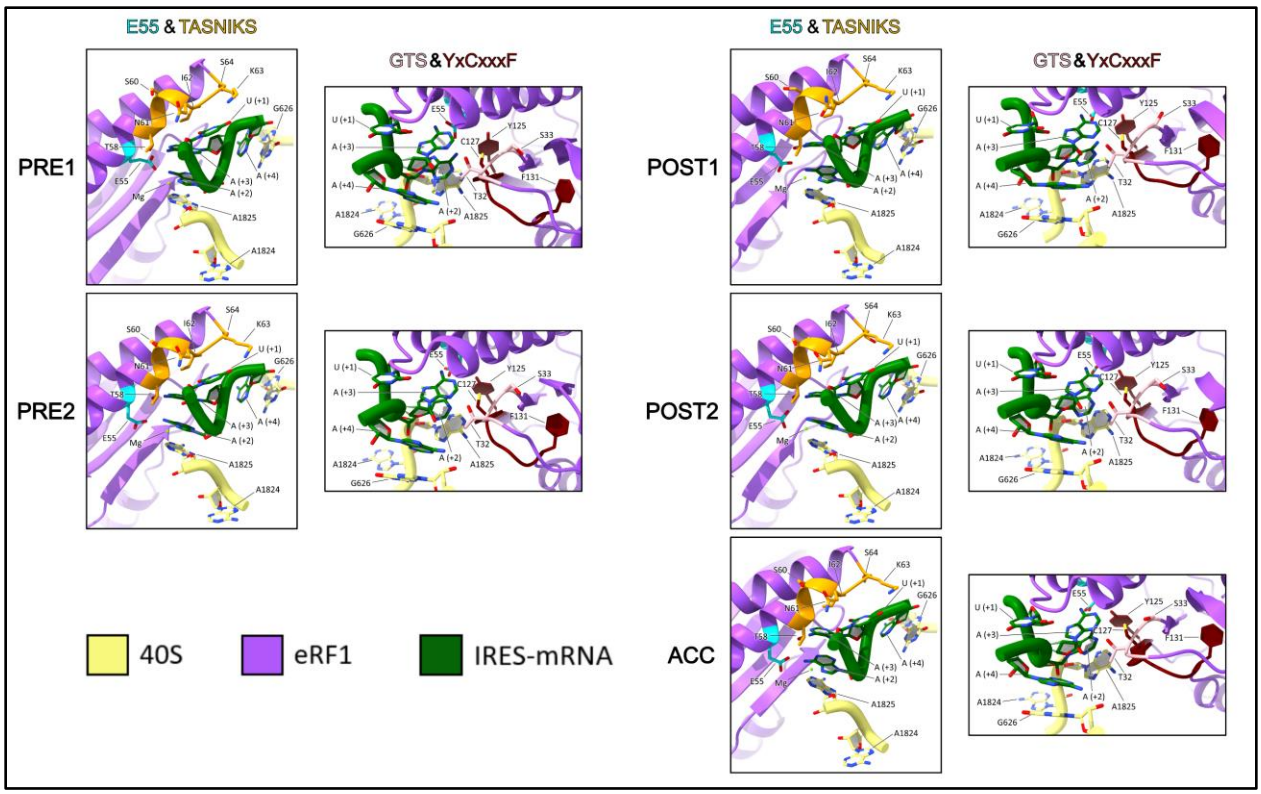

Figure 18. eRF1-stop codon interactions. The stop codon adopts a compact conformation and interacts with E55 and the residues of the TASNIKS, GTS, and YxCxxxF motifs of eRF1. Structures were aligned by the 28S rRNA.

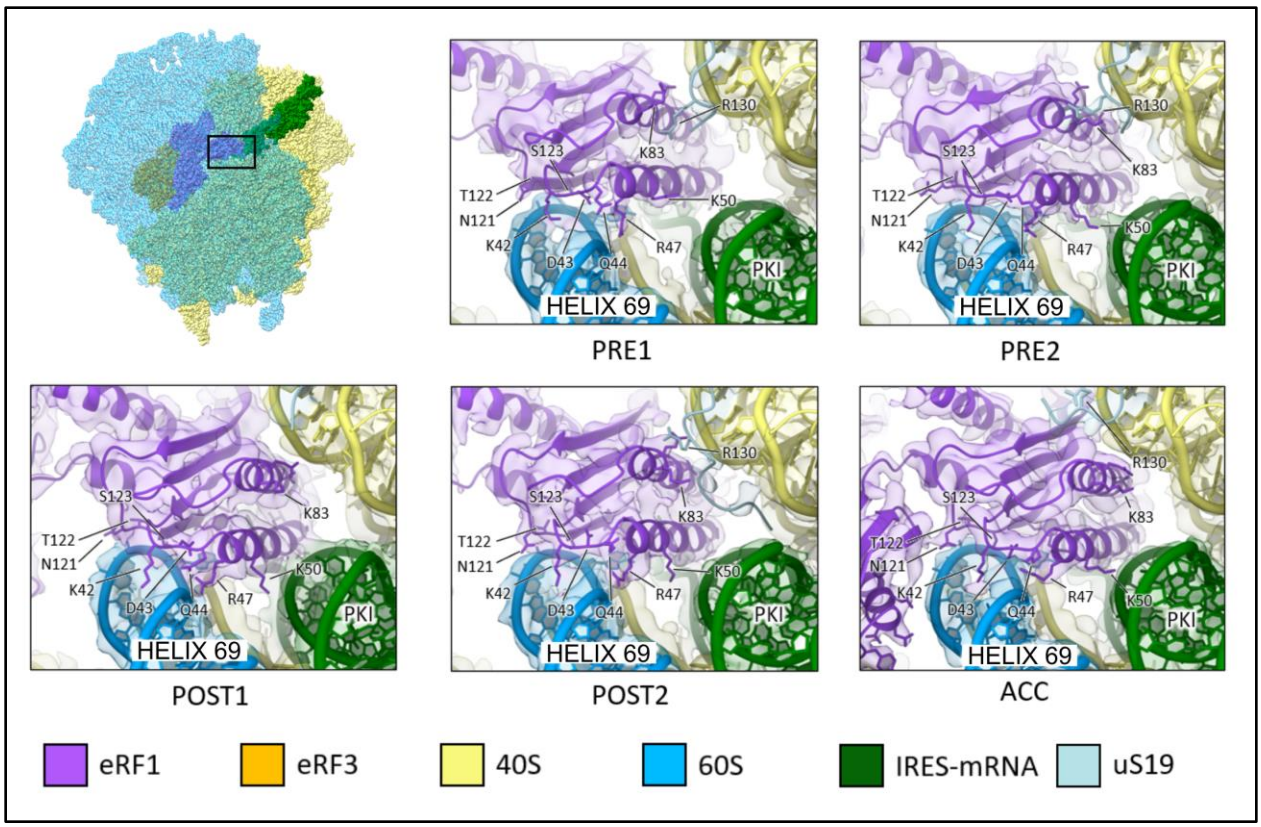

Figure 19. eRF1-NTD interactions with helix 69 of the 28S rRNA and PKI. Structures and maps were aligned by the 28S rRNA.

C-terminal domain

The C-terminus of eRF1 docks against the GTPase-associated center (GAC) interacting primarily with H43-44 of the 28S rRNA and ribosomal protein uL11. The density for this region is not very clear, but the close interactions are primarily mediated by the residues in the unstructured C-terminal loop of eRF1. D418 of eRF1 C-terminus is within hydrogen bonding distance of T25 of uL11 in the LSU for PRE1, PRE2, POST1, and POST3. In ACC, T25 of uL11 forms two interactions with the eRF1 C-terminal residues. The backbone of T25 interacts with the backbone carbonyl of E313 and the side chain of T25 interacts with the backbone carbonyl of F348 in the eRF1 C-terminus, respectively. Additionally, Y415 of eRF1 stacks with G1920 of

28S rRNA in the pre-accommodation states (PRE1, PRE2, POST1, and POST2) and with G1948 in the post-accommodation state (ACC) (**Figure 15**). Similar stacking interactions are also formed by tRNA during the elongation cycle [36]. The encroachment of eRF1 towards the A site pushes the GAC away from the SSU by ~2.7 Å. GAC undergoes a large motion of ~14 Å towards the helix 89 of the 28S rRNA in ACC as eRF3 dissociates and eRF1 gets accommodated into the PTC after GTP hydrolysis.

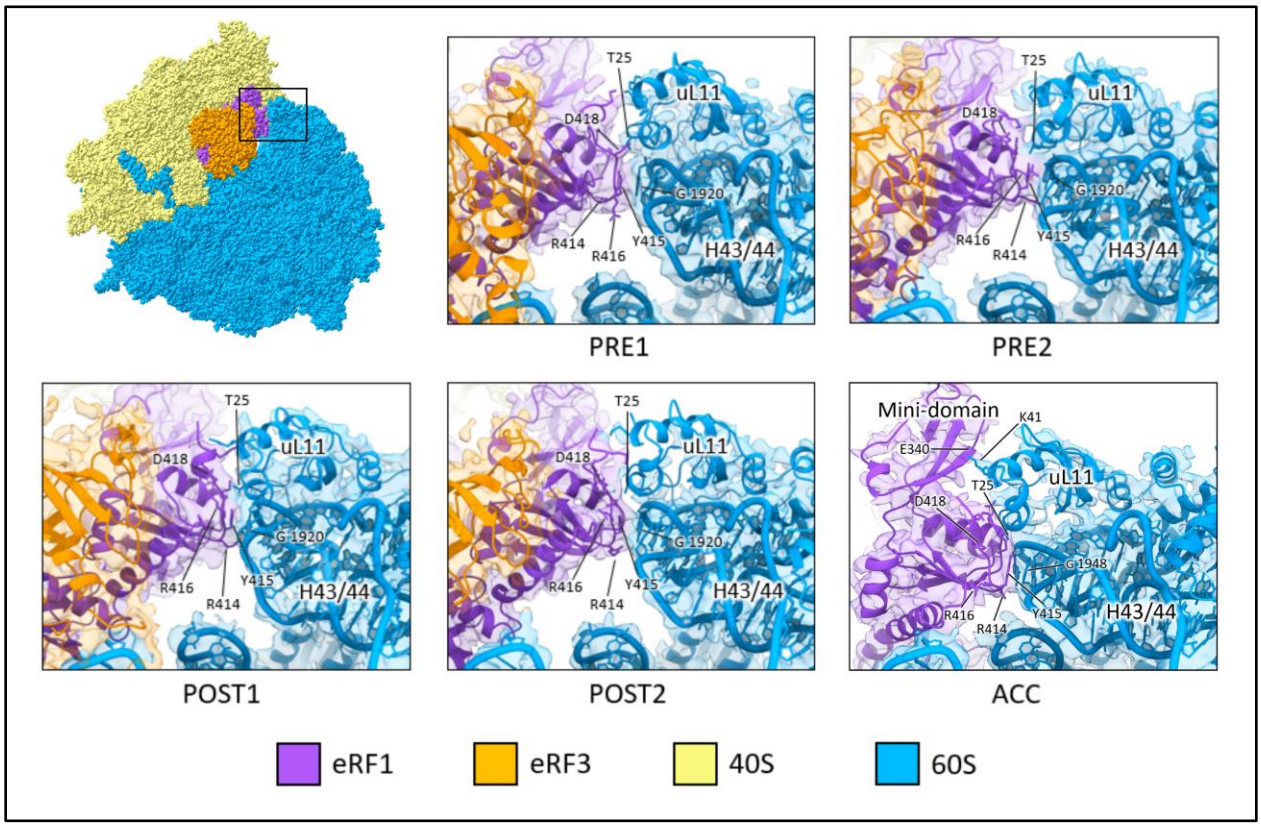

Figure 20. eRF1-CTD interactions with the H43/44 and uL11 of the GAC. Structures and maps were aligned by the 28S rRNA.

The dynamic mini domain interacts with the SSU head in PRE1, PRE2, POST1, and POST2. The exact interactions are unclear in the maps but primarily take place between the N-

terminus (residues Y85, K89, and N91) of the SSU ribosomal protein eS31 and the flexible loops Q364-E367 and C335-T338 of the eRF1 mini domain. In ACC, the mini domain moves away from the SSU and interacts with the LSU ribosomal protein uL11 via hydrogen bonding between E340 of eRF1 and K41 of uL11 (**Figure 15**).

M-domain

The M-domain of eRF1 remains bound to eRF3 through most of the termination process. The domain sits in the cleft between the LSU and SSU (**Figure 17**) and only enters the PTC after eRF3 has dissociated. The interactions between eRF3 and the M-domain of eRF1 are the same as described in **Section 1.7.2** and remain stable in classes PRE1, PRE2, and POST1. These interactions likely play a key role in the proper positioning of eRF3 for GTPase activation. In POST2, the G-domain becomes disordered weakening the interactions between eRF3 and the M-domain. In ACC, the M-domain undergoes large motion using the NTD as a pivot point. The helices α8 and α9, which were held at a kink in the pre-termination structures, straighten to form a continuous helix. This results in the tip of the α5 helix harboring the catalytic GGQ motif to undergo a displacement of ~80Å and place near the peptide exit tunnel in the PTC (**Figure 16**). The CTD also swings away from the head of the SSU and closer to the GAC. Muhs et al mention eukaryotic-specific interactions between domain M of PTC-accommodated eRF1 and helix 71 of the 28S rRNA around S253 and A226 of eRF1 and G3761 and C3758 of helix 71 [6]. We do see multiple interactions around the mentioned region in ACC. O2’ of the C3758 sugar backbone hydrogen bonds with the side chains of D152 and S154 and the backbone nitrogen of S154. A230 backbone nitrogen hydrogen bonds with the phosphate backbone of U3762. S257

backbone carbonyl hydrogen bonds with O2' of G3761 sugar backbone. We also see a stacking interaction between T258 and C3779.

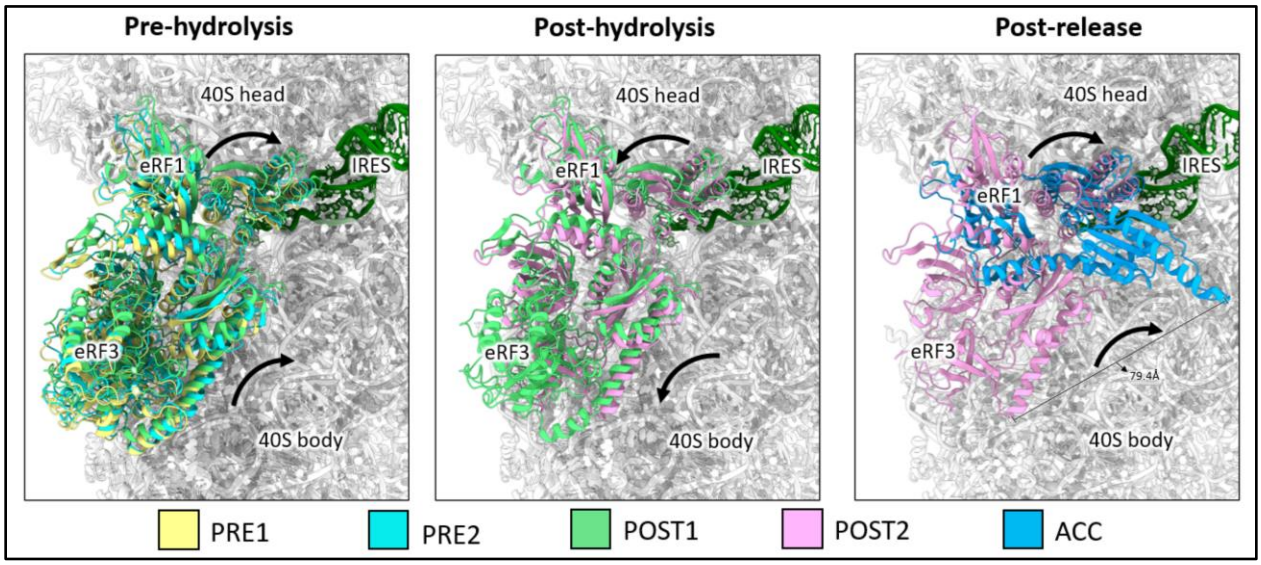

Figure 21. Overall motion of the RFs during the termination process as viewed from the interface side of the SSU (LSU is hidden for clarity). Pre-hydrolysis, eRF1 moves further into the A site dragging eRF3 along. Post-hydrolysis, the G-domain of eRF3 becomes disordered indicating GDP release. eRF3 slowly dissociates pulling eRF1 away from the A site. Post-eRF3-release, the M-domain of eRF1 moves by almost 80Å and gets accommodated into the PTC. Structures were aligned by the 28S rRNA.

Comparison of the accommodated eRF1 M-domain with a previously published structure

Overlay of the eRF1's M-domain from ACC on a previous structure of PTC accommodated eRF1 (GGQ to AAQ) mutant [3] reveals the differences in conformation arising from using a tRNA mimic with an empty P-site. The core of the M-domain made primarily of beta-sheets is positioned similarly between the two structures. The long α5 helix harboring the catalytic GGQ

motif at its tip is shifted by ~1.4 Å towards the P-site compared to the published structure. This is likely due to the absence of a P-site tRNA in ACC, which occupies additional space in the PTC in the published structure. The loop region immediately preceding the GGQ motif is also displaced in ACC compared to the published structure. The displacement seems to be caused by the different conformations of A4294 of the 28S rRNA, which lies perpendicular to the α5 helix axis in ACC but gets flipped parallel to the α5 helix axis when a P-site tRNA is present. The other nearby elements of the PTC are similar between the two structures (**Figure 17**).

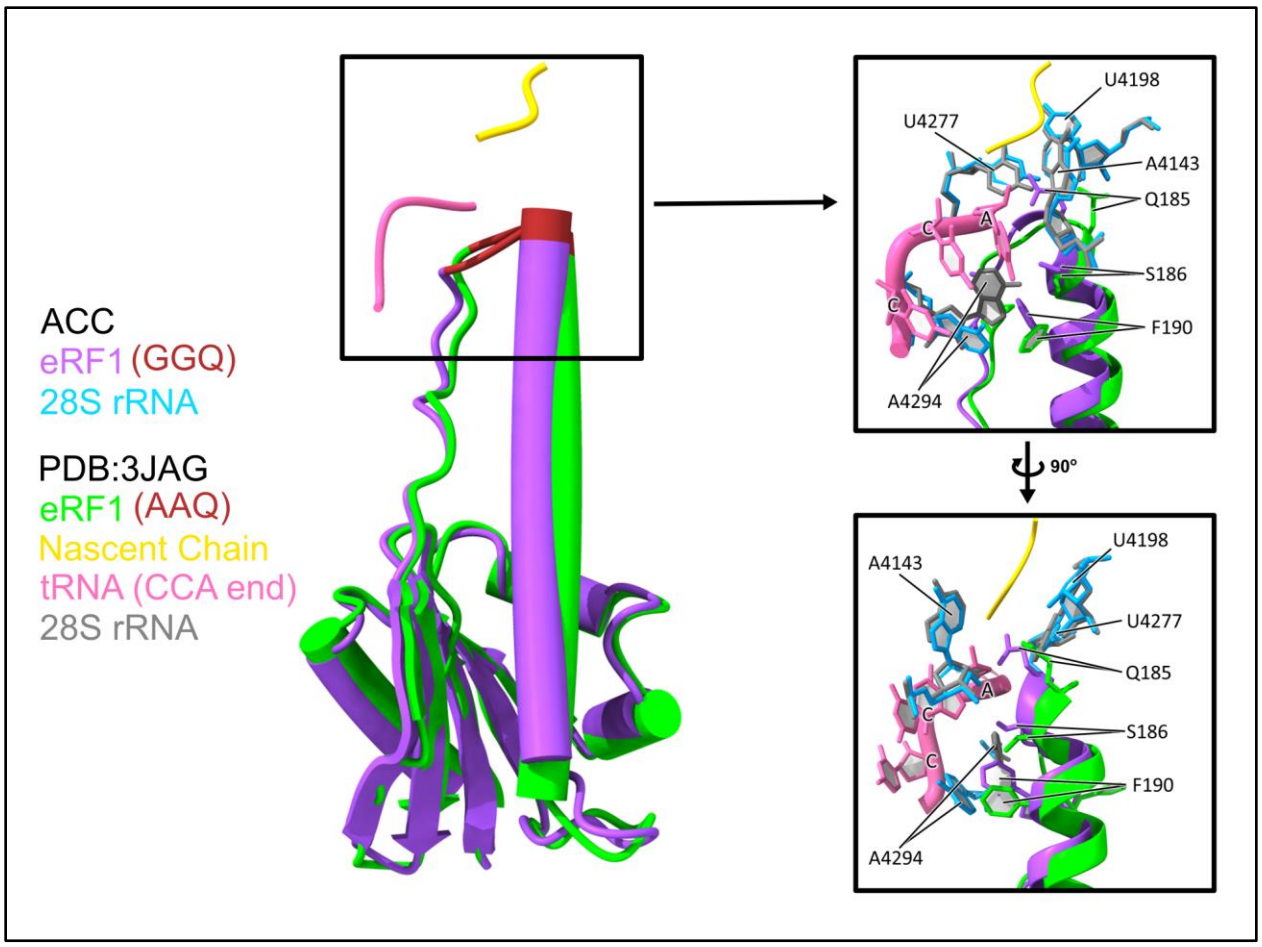

Figure 22. Comparison of eRF1's M-domain from the ACC class with a previously published structure (PDB:3JAG) [3]. Structures were aligned by the 28S rRNA.

4.3.4 eRF3 conformations during termination

Interactions with the SSU

eRF3 interacts with the SSU at three locations. The first interaction is between ribosomal protein uS12 C-terminus and domains II and III of eRF3. The interaction takes place via T600 of eRF3 and S143 of uS12 in PRE2, POST1, and POST2, but is absent in PRE1. The second interaction involves helix 5 of 18S rRNA and loop D450-G452 of eRF3 domain II. In PRE1, the interaction is weak and primarily through Van der Waals interactions with M451. The

interactions become stronger in PRE2, POST1, and POST2 as domain II moves closer to allow hydrogen bonding between the phosphate backbone of G478 in helix 5 of the 18S rRNA and the backbone nitrogen of G452 in domain II of eRF3. The third interaction is via the stacking of A464 in helix 14 of the 18S rRNA with R242 of eRF3 as well as hydrogen bonding between the phosphate backbone of A464 with the K246 side chain. This interaction is absent in POST2. The weak to non-existent interactions between eRF3 and the SSU in PRE1 suggest that the ternary complex initially binds to the ribosome primarily through eRF1 with eRF3 anchoring only after stop codon recognition.

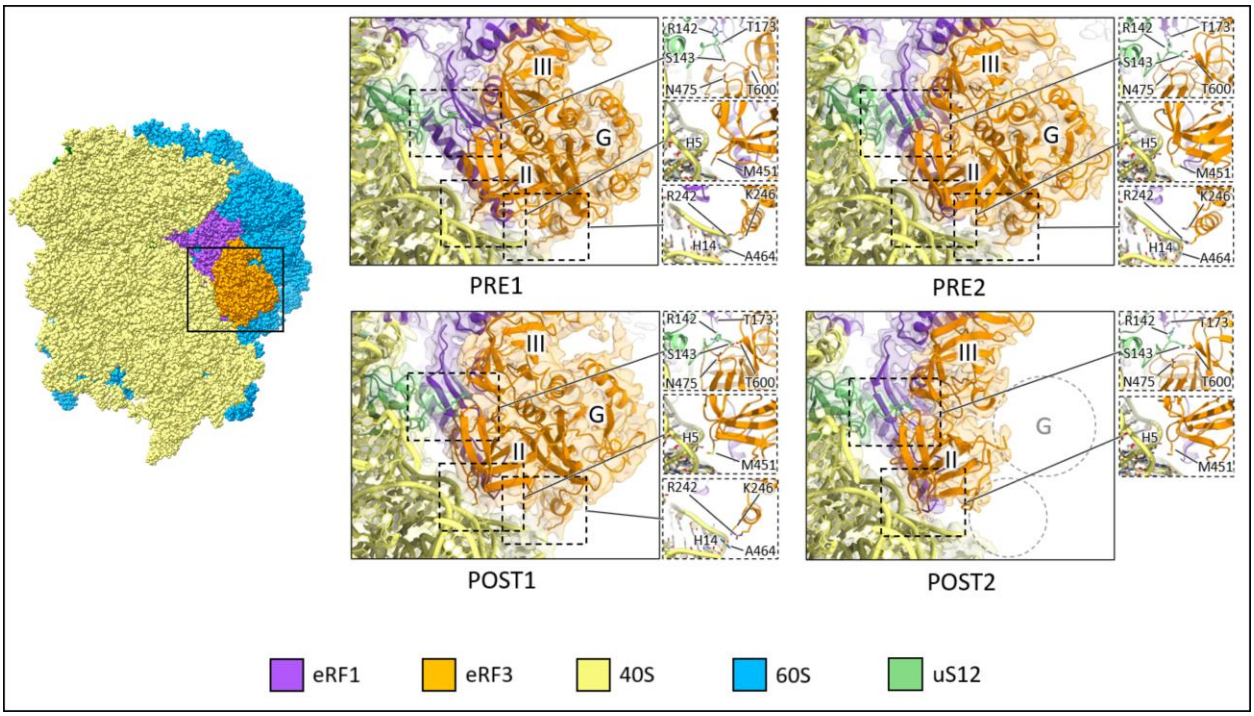

Figure 23. eRF3 anchoring and subsequent interactions with the SSU. Structures and maps were aligned by the 28S rRNA.

Interactions with the Sarcin-ricin loop

The encroachment of eRF1 into the A site drags eRF3 along and places the G-domain closer to the catalytic SRL. The catalytic histidine H300 in the switch 2 loop of the eRF3 G-domain interacts with A4353 of the SRL in classes PRE1, PRE2, and POST1. The histidine is poised to coordinate a water molecule necessary for carrying out GTP hydrolysis [36], but the water molecule is not visible in our maps. Motion of eRF3 towards the SRL in POST1 causes the catalytic histidine to flip towards the GTP binding pocket triggering GTP hydrolysis (**Figures 18 and 20**).

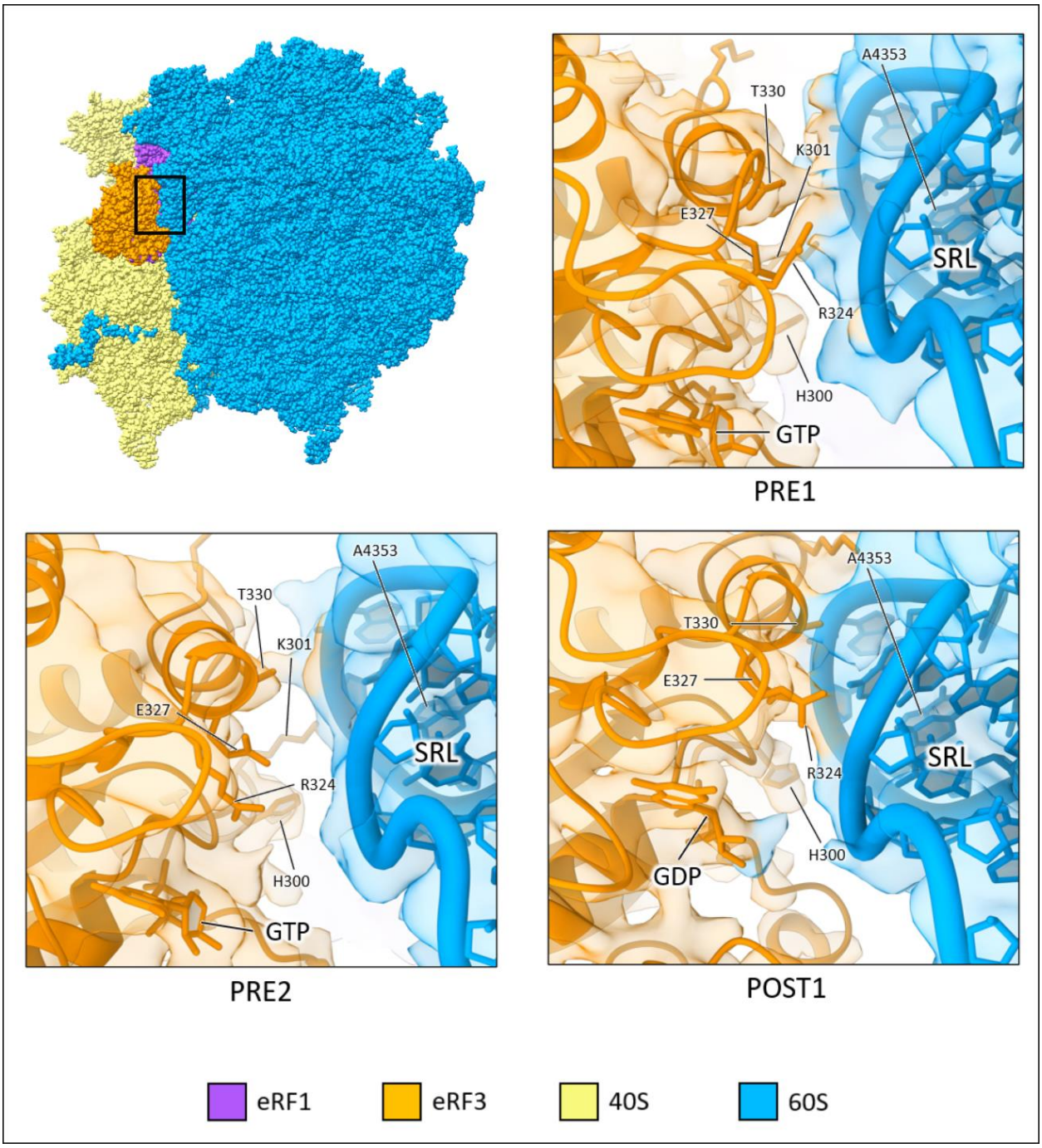

Figure 24. eRF3 G-domain interactions with the SRL. The interactions are non-existent in PRE1 and PRE2. The interactions mainly occur in POST1 as the G-domain gets pressed against the SRL. Key interaction takes place between the catalytic H300 and the phosphate backbone of A4353 of the SRL. Structures and maps were aligned by the 28S rRNA.

G-domain

G-domain undergoes multiple changes during the termination process. PRE1 and PRE2 contain a structured Switch 1 region, which sits at the interface of the LSU and SSU interacting with H14 of the 18S rRNA. eRF3 motion in POST3 causes clashes between Switch 1 and the NTD of uL14 resulting in the partial disorder of the region (**Figure 19**). The disorder likely plays an important role in the dissociation of GDP post-hydrolysis. The G-domain is entirely disordered in the POST2 state suggesting GDP release has likely taken place. Switch1 region becomes disordered upon GTP hydrolysis in bacterial elongation complexes trapped using kirromycin [115, 116], but remains intact in eEF1A during eukaryotic elongation even post-Pi release as shown by didemnin B stalled complexes [11]. Switch 1 disorder has been thought to be a gating mechanism facilitating GTPase dissociation post-GTP hydrolysis [117,118]. Our structures show that Pi release alone does not trigger the disorder of switch 1 on its own. Instead, the disorder is triggered due to steric clashes between switch 1 and uL14 N-terminus. This disorder likely destabilizes the bound GDP and results in its dissociation from eRF3. The G-domain seems to become disordered after GDP dissociation.

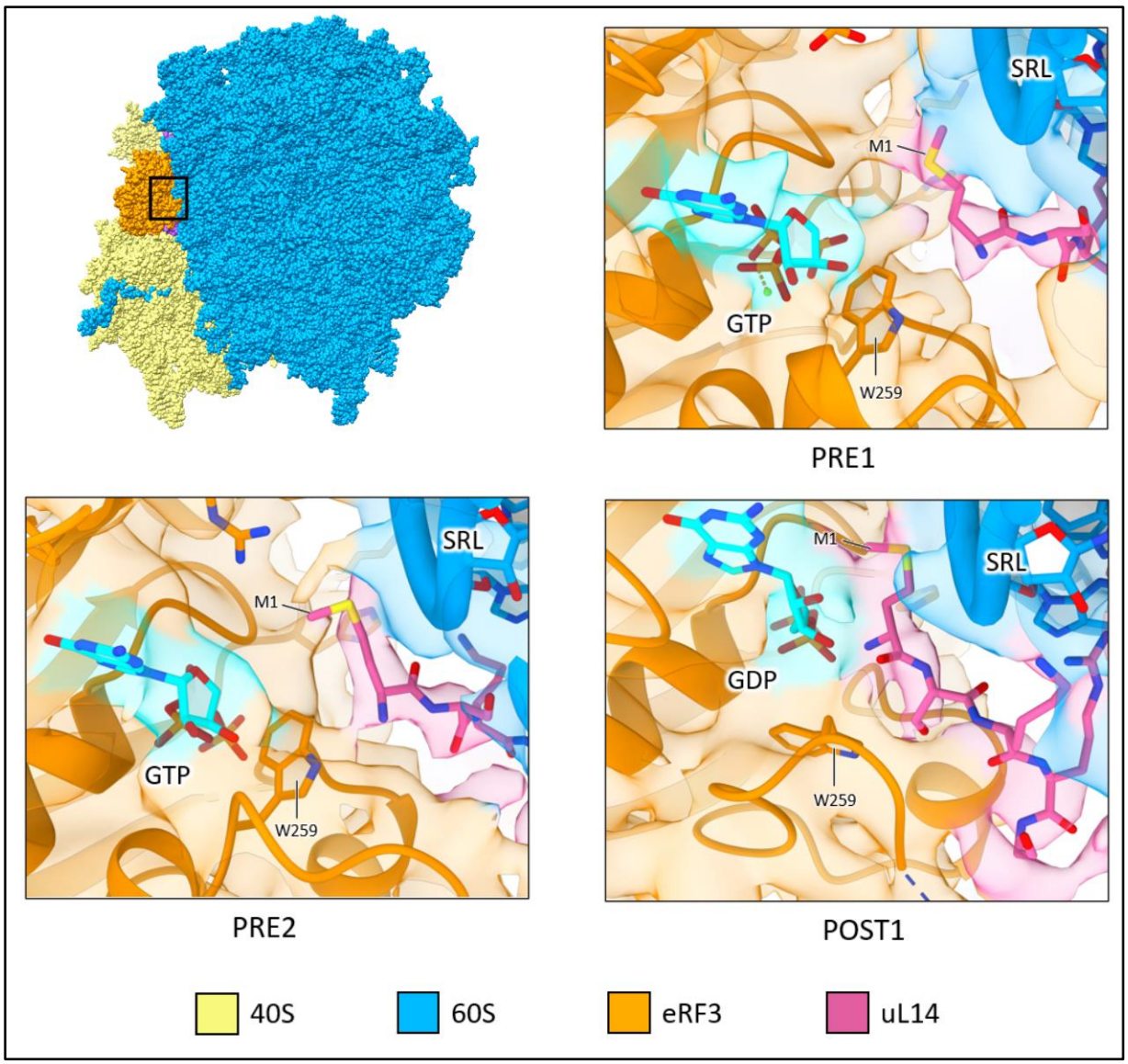

Figure 25. N-terminus of ribosomal protein uL14 extends into the GTP-binding pocket of the eRF3 G-domain. Structures and maps were aligned by the 28S rRNA.

4.3.5 Visualization of GTP hydrolysis steps

Overall mechanism of GTP hydrolysis

The structures allowed us to identify the hydrolysis state of GTP bound to the eRF3 and build the surrounding regions (**Figure 20**). PRE1 has density for GTP coordinating a magnesium ion, similar to previous structures for translational GTPases (eEF1A and eRF3) [8, 36]. The catalytic histidine H300 located in the switch 2 region is flipped away in an inactive state. Density for the α3 helix of the switch 1 region is clear with W259 docked against the GTP molecule, but the α4 helix is partially disordered. Additional density near the switch 1 region, attributed to W259 in the previously published structure [3], was instead assigned to the NTD of ribosomal protein uL14. The N-terminal region of uL14 snakes around the α2 and α3 helices and places its N-terminus close to W259, potentially forming a hydrogen bond.

PRE2 state has a clear density for GTP, but the density for magnesium is missing. The catalytic histidine is still flipped away suggesting it to be a pre-GTPase-activation state. The release of magnesium suggests that the hydrolysis process is magnesium-independent. Binding analysis has shown that magnesium is conducive to GTP binding but detrimental to GDP binding [93]. The release of magnesium during the GTPase activation process could facilitate the GTP to GDP transition. Densities for the α3 helix of switch 1 and uL14 are similar to the ones observed in PRE1. The density for the α4 helix becomes clearer and matches the previously published structure [3]. The improved density could be due to better anchoring with the ribosome or magnesium release.

POST1 state has density for GDP with no additional density to fit a γ-phosphate, P, or magnesium. The switch 2 region is pressed against the SRL flipping the catalytic histidine

towards the nucleotide-binding pocket thereby activating the GTPase. The large motion of eRF3 towards the SRL also causes the α2 and α3 helices to clash against the N-terminal region of uL14. This in turn results in disorder of the switch 1 region and likely facilitates GDP release. The W259 is also flipped downwards resulting in the opening of the nucleotide-binding pocket for GDP release.

POST2 state has disordered density for the G-domain and likely represents a post-GDP release state of eRF3. The domains II and III are still bound to the M-domain of eRF1 preventing its accommodation into the PTC. The densities of domains II and III are also somewhat disordered suggesting a weakening of interactions with eRF1. eRF1 accommodation likely occurs concurrently with eRF3 release as we do not observe any additional intermediate states.

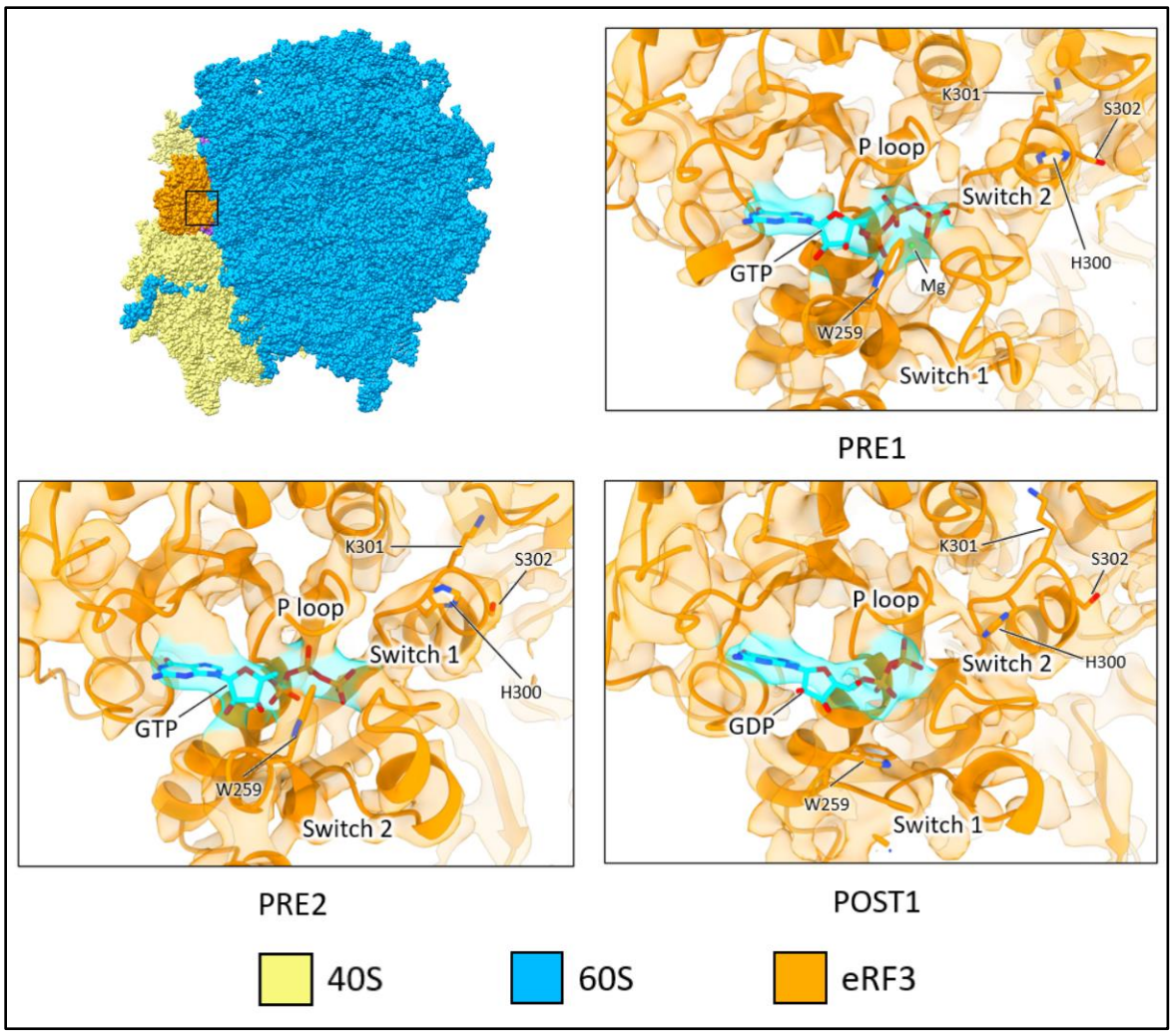

Figure 26. GTP-binding pocket of eRF3 during the termination process. Structures and maps aligned by the G-domain of eRF3.

Comparison with previous structures

Comparison of the pre-termination structures obtained in this study with a previously published structure of a GMPPCP stalled pre-termination complex [11] provides further evidence supporting the chronological order assigned to the different classes. eRF3 binding location in POST1 resembles the previously published structure most closely with backbone root mean square deviation (RMSD) of 2.04Å. This makes sense as the non-hydrolysable GMPPCP

stalls the complex right before the hydrolysis stage. PRE1 has the most distant binding location for eRF3 compared to the published structure with a backbone RMSD of 6.62Å, and PRE2's eRF3 binding location falls in between the two mentioned previously with a backbone RMSD of 3.69Å. A closer look at the nucleotide-binding pockets shows the binding modes for GTP, GMPPCP, and GDP in eRF3. Both GTP and GMPPCP coordinate a magnesium atom using their β and γ oxygens. Interestingly, in the GTP structure, S226 coordinates the magnesium whereas in the GMPPCP structure, T277 coordinates the magnesium. Both S21 (equivalent to S226 in eRF3) and T72 (equivalent to T277 in eRF3) coordinate the magnesium in the eEF1A nucleotide binding pocket occupied by GTPγS [36]. Whether the differences in magnesium coordinating residues arise from the use of different GTP analogs or due to the different conformations of the G-domain is still unclear.

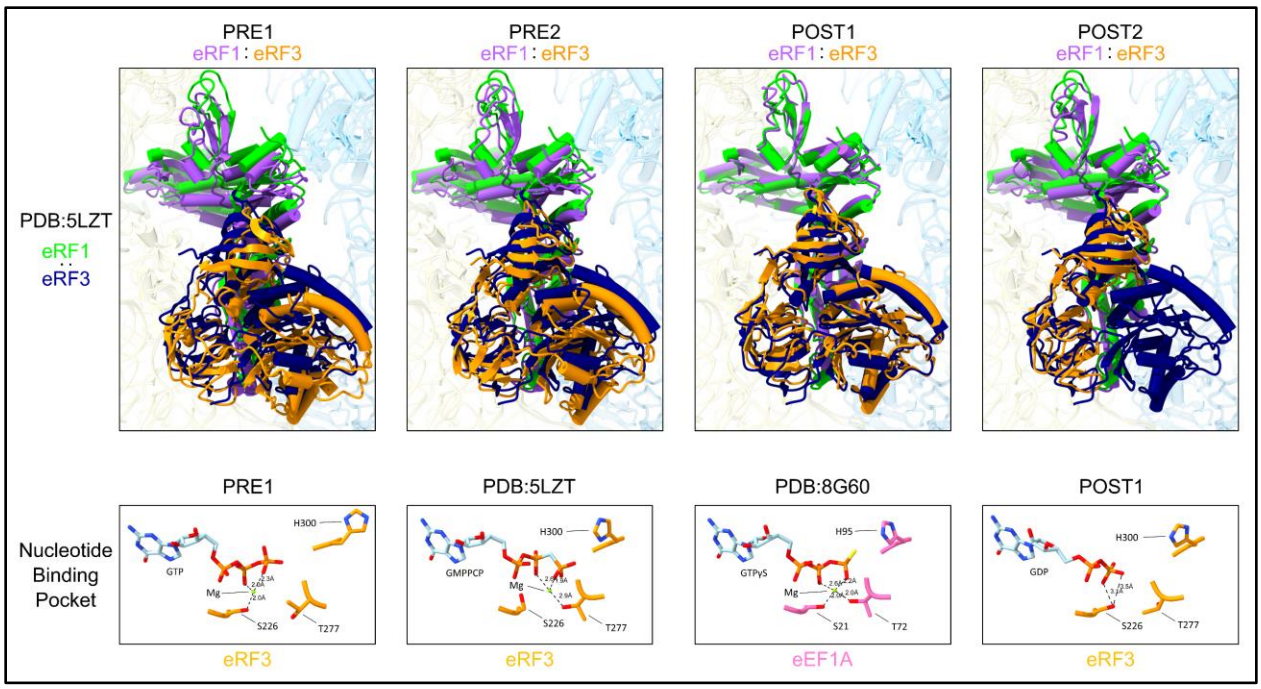

Figure 27. Comparison of the overall conformation of the pre-termination complex stalled using GMPPCP (PDB:5LZT) with the pre-termination complexes obtained in our study (top) and the local stereochemistry for eRF3:GTP in PRE1, eRF3:GMPPCP in PDB:5LZT, eEF1A:GTPγS in PDB:8G60, and eRF3:GDP in POST1 (bottom). Structures were aligned using the 28S rRNA for top panels and using the G-domains of the respective GTPases for the bottom panels.

Chapter 5: Conclusion

5.1 TRCEM for capturing structural intermediates

As part of this work, we developed modular PDMS-based microfluidic devices with a SiO_2 coated 3D SAR-micromixer, a glass capillary for reaction channel, and a 3D micro-sprayer. The modular design allows for easy disassembly and reuse of the three different parts, making the fabrication process much easier. The SiO_2 coating provides a pristine and hydrophilic environment for biochemical reactions. These devices are excellent for capturing biochemical reactions in the range of 10 ms to 1000 ms. We used these devices in addition to on-grid mixing, and conventional blotting methods for capturing intermediates formed during eukaryotic translation termination at multiple time points ranging from 400 ms to 10 min. The TRCEM experiments resulted in five different structures, four of which were for intermediates formed during the termination process. Population analysis showed that using microfluidic mixing performs better than on-grid mixing. These results showcase the advantages of using microfluidic mixing-spraying and the modular microfluidic design. The ease of use introduced by the modular design will hopefully make microfluidic TRCEM more accessible and allow its use for studying various biological molecules. We also point out some of the remaining issues with the current TRCEM methods. The microfluidic devices allow for fast and efficient mixing, but suffer from residence time dispersion due to laminar flow. Analytical models for this time dispersion are available, but they have not yet been incorporated into the kinetic models for better interpretation of population results. There also seems to be a gap in the reaction times achievable by the current TRCEM methods. The microfluidics-based methods are limited between 10 ms and 2000 ms reaction times by the plunging time on the lower end and the

increasing chip volume on the higher end. On-grid mixing and reaction is similarly limited to a minimum reaction time of ~10 s due to the limitations imposed by pipetting, blotting, and plunging. This leaves a gap between 2 s and 10 s, where there are no methods for TRCEM sample preparation. Hopefully methods are developed in the future to address this gap.

5.2 TRCEM captures structural intermediates for mammalian translation termination

Using TRCEM, we solved the structures of four intermediates formed during mammalian translation termination. The structures show that stop codon recognition happens before anchoring of eRF3 to the SSU. This likely facilitates the unbinding of the RFs in case of improper decoding events. Unfortunately, the steps for stop codon decoding by eRF1 were not captured in our experiments. TRCEM experiments with shorter reaction times are needed to capture the stop codon decoding process. Successful stop codon decoding anchors one end of eRF1's NTD to the A site and acts as a pivot point for eRF1's further incursions into the A site. eRF1 forms multiple hydrogen bonding interactions with the ribosome which are weaker upon initial binding and get stronger as eRF1 moves deeper into the A site. The increased interactions likely act as a driving force in propagating the termination process. The movements of eRF1 towards the A site are translated to eRF3. The movement presses the G-domain of eRF3 against the SRL causing the catalytic histidine H300 to flip towards the nucleotide-binding pocket and hydrolyzing the bound GTP. The limited resolution near the GTP binding pocket prevented us from visualizing any water molecules near the active site. Higher resolution structures are needed to resolve the water molecules responsible for coordinating the GTP bound magnesium and interacting with the nearby residues of the active site.

Interestingly, magnesium was only observed to bind alongside GTP in the earliest class, PRE1. The subsequent classes had no density for magnesium, but GTP/GDP was still bound. Magnesium was absent in the PRE2 class, which had the catalytic H300 flipped away from the nucleotide-binding pocket, suggesting it to be a pre-GTPase activation class. The release of magnesium before GTP-hydrolysis points towards a magnesium-independent GTP-hydrolysis mechanism. Further investigation is needed to confirm these findings.

After hydrolysis, GDP stays bound to eRF3. The switch1 region, thought to be the gating mechanism for GDP release remains ordered. Our structures reveal a mechanism resulting in the disorder of the switch 1 region. The N-terminus of ribosomal protein uL14 interacts with the switch 1 loop throughout the termination process. As eRF3 gets pressed against the SRL, the switch1 region also gets pressed against the N-terminus of uL14. This clash likely disrupts the switch 1 region leading to its disorder and consequently GDP release. Biochemical and mutational analysis of the N-terminus of uL14 is needed to further understand its role in termination.

Post-GDP-release, eRF3's G-domain becomes disordered. The domains II and II remain bound to eRF1 keeping it in a pre-accommodation state. eRF3 dissociation and eRF1's accommodation into the PTC likely take place concurrently as we did not observe any additional intermediates. Single-molecule fluorescence experiments can be used to further investigate the accommodation process.

References

1. Frolova, L., Goff, X.L., Rasmussen, H.H., Cheperegin, S., Drugeon, G., Kress, M., Arman, I., Haenni, A.L., Celis, J.E., Philippe, M., Justesen, J., Kisselev, L., A highly conserved eukaryotic protein family possessing properties of polypeptide chain release factor. Nature 372, 701–703 (1994).
2. Alkalaeva, E.Z., Pisarev, A.V., Frolova, L.Y., Kisselev, L.L., Pestova, T.V., In vitro reconstitution of eukaryotic translation reveals cooperativity between release factors eRF1 and eRF3. Cell 125, 1125–1136 (2006).
3. Brown, A., Shao, S., Murray, J., Hegde, R.S., Ramakrishnan, V., Structural basis for stop codon recognition in eukaryotes. Nature 524, 493–496 (2015).
4. des Georges, A., Hashem, Y., Unbehaun, A., Grassucci, R.A., Taylor, D., Hellen, C.U., Pestova, T.V., Frank, J., Structure of the mammalian ribosomal pre-termination complex associated with eRF1.eRF3.GDPNP. Nucleic Acids Res. 42(5), 3409-3418 (2014).
5. Matheisl, S., Berninghausen, O., Becker, T., Beckmann, R., Structure of a human translation termination complex. Nucleic Acids Res. 43(18), 8615-8626 (2015).
6. Muhs, M., Hilal, T., Mielke, T., Skabkin, M.A., Sanbonmatsu, K.Y., Pestova, T.V., Spahn, C.M., Cryo-EM of ribosomal 80S complexes with termination factors reveals the translocated cricket paralysis virus IRES. Mol. Cell 57(3),422-432 (2015).
7. Shoemaker, C.J., and Green, R., Kinetic analysis reveals the ordered coupling of translation termination and ribosome recycling in yeast. Proc. Natl. Acad. Sci. U.S.A. 108, E1392–E1398 (2011).

8. Eyler, D.E., Wehner, K.A., Green, R., Eukaryotic release factor 3 is required for multiple turnovers of peptide release catalysis by eukaryotic release factor 1. J. Biol. Chem. 288, 29530–29538 (2013).
9. Zhouravleva, G., Frolova, L., Goff, X.L., Guellec, R.L., Inge-Vechtomov, S., Kisselev, L., Philippe, M., Termination of translation in eukaryotes is governed by two interacting polypeptide chain release factors, eRF1 and eRF3. EMBO J. 14, 4065–4072 (1995).
10. Lawson, M.R., Lessen, L.N., Wang, J., Prabhakar, A., Corsepius, N.C., Green, R., Puglisi, J.D., Mechanisms that ensure speed and fidelity in eukaryotic translation termination. Science 373, 876-882 (2021).
11. Shao, S., Murray, J., Brown, A., Taunton, J., Ramakrishnan, V., Hegde, R.S., Decoding Mammalian Ribosome-mRNA States by Translational GTPase Complexes. Cell 167(5), 1229-1240 (2016).
12. Preis, A., Heuer, A., Barrio-Garcia, C., Hauser, A., Eyler, D.E., Berninghausen, O., Green, R., Becker, T., Beckmann, R., Cryoelectron Microscopic Structures of Eukaryotic Translation Termination Complexes Containing eRF1-eRF3 or eRF1-ABCE1. Cell Reports 8(1), 59-65 (2014).
13. Chen, B., Kaledhonkar, S., Sun, M., Shen, B., Lu, Z., Barnard, D., Lu, T.M., Gonzalez, R.L. Jr., Frank, J., Structural dynamics of ribosome subunit association studied by mixing-spraying time-resolved cryogenic electron microscopy. Structure 23(6), 1097-105 (2015).
14. Frank, J., Time-resolved cryo-electron microscopy: Recent progress. 647 J. Struct. Biol. 200, 303-306 (2017).

15. Chen, B., and Frank, J., Two promising future developments of cryo-EM: capturing short-lived states and mapping a continuum of states of a macromolecule. Microscopy (Oxf.) 65, 69-79 (2016).
16. Lu, Z., Shaikh, T.R., Barnard, D., Meng, X., Mohamed, H., Yassin, A., Mannella, C.A., Agrawal, R.K., Lu, T.M., Wagenknecht, T., Monolithic microfluidic mixing-spraying devices for time-resolved cryo-electron microscopy. J. Struct. Biol. 168, 388-395 (2009).
17. Berriman, J., and Unwin, N., Analysis of transient structures by cryo-electron microscopy combined with rapid mixing of spray droplets. Ultramicroscopy 56(4), 241-252 (1994).
18. Kontziampasis, D., Klebl, D.P., Iadanza, M.G., Scarff, C.A., Kopf, F., Sobott, F., Monteiro, D.C.F., Trebbin, M., Muench, S.P., White, H.D., A cryo-EM grid preparation device for time-resolved structural studies. IUCrJ 6, 1024-1031 (2019).
19. Maeots, M.E., Lee, B., Nans, A., Jeong, S.G., Esfahani, M.M.N., Ding, S., Smith, D.J., Lee, C.S., Lee, S.S., Peter, M., Enchev, R.I., Modular microfluidics enables kinetic insight from time-resolved cryo-EM. Nat. Commun. 11, 3465 (2020).
20. Klebl, D.P., White, H.D., Sobott, F., Muench, S.P., On-grid and in-flow mixing for time-resolved cryo-EM. Acta Crystallogr. D Struct. Biol. 77, 1233-1240 (2021).
21. Kaledhonkar, S., Fu, Z., White, H., Frank, J., Time-Resolved Cryo-electron Microscopy Using a Microfluidic Chip. Methods Mol. Biol. 1764, 59-71 (2018).
22. Lu, Z., Barnard, D., Shaikh, T.R., Meng, X., Mannella, C.A., Yassin, A., Agrawal, R., Wagenknecht, T., Lu, T.M., Gas-Assisted Annular Microsprayer for Sample Preparation for Time-Resolved Cryo-Electron Microscopy. J. Micromech. Microeng. 24, 115001 (2014).

23. Mäeots, M.E., and Enchev, R. I., Structural dynamics: review of time-resolved cryo-EM. Acta Cryst. D 78, 927–935 (2022).

24. Murray R.F., Harper H.W., Granner D.K., Mayes P.A., Rodwell V.W., Harper's Illustrated Biochemistry. New York: Lange Medical Books/McGraw-Hill (2006). ISBN 978-0-07-146197-9.

25. Crick, F., Central Dogma of Molecular Biology. Nature 227, 561–563 (1970).

26. Brown, A., Baird, M.R., Yip, M.C., Murray, J., Shao, S., Structures of translationally inactive mammalian ribosomes. eLife 7, e40486 (2018).

27. Fedry, J., Silva, J., Vanevic, M., Fronik, S., Mechulam, Y., Schmitt, E., des Georges, A., Faller, W., Förster, F., Visualization of translation reorganization upon persistent collision stress in mammalian cells. bioRxiv (2023) doi: 10.1101/2023.03.23.533914.

28. Klinge, S., Voigts-Hoffmann, F., Leibundgut, M., and Ban, N., Atomic structures of the eukaryotic ribosome. Trends Biochem. Sci. 37, 189–198 (2012).

29. Agrawal, R.K., Spahn, C.M., Penczek, P., Grassucci, R.A., Nierhaus, K.H., and Frank, J., Visualization of tRNA movements on the Escherichia coli 70S ribosome during the elongation cycle. J. Cell. Biol. 150, 447-460 (2000).

30. Schmeing, T., Ramakrishnan, V., What recent ribosome structures have revealed about the mechanism of translation. Nature 461, 1234–1242 (2009).

31. Carbone, C.E., Loveland, A.B., Gamper, H.B., Hou, Y.M., Demo, G., Korostelev, A.A., Time-resolved cryo-EM visualizes ribosomal translocation with EF-G and GTP. Nat. Commun. 12, 7236 (2021).

32. Loveland, A.B., Demo, G., Korostelev, A.A., Cryo-EM of elongating ribosome with EF-Tu•GTP elucidates tRNA proofreading. Nature 584, 640–645 (2020).

33. Petrychenko, V., Peng, B.Z., de A. P. Schwarzer, A.C., Peske, F., Rodrina, M.V., Fischer, N., Structural mechanism of GTPase-powered ribosome-tRNA movement. Nat. Commun 12, 5933 (2021).

34. Dever, T.E., and Green, R., The elongation, termination, and recycling phases of translation in eukaryotes. Cold Spring Harb. Perspect. Biol. 4, 1–16 (2012).

35. Juette, M.F., Carelli, J.D., Rundlet, E.J., Brown, A., Shao, S., Ferguson, A., Wasserman, M.R., Holm, M., Taunton, J., Blanchard, S.C., Didemnin B and ternatin-4 differentially inhibit conformational changes in eEF1A required for aminoacyl-tRNA accommodation into mammalian ribosomes. eLife 11, e81608 (2022).

36. Holm, M., Natchiar, S.K., Rundlet, E.J., Myasnikov, A.G., Watson, Z.L., Altman, R.B., Wang, H.Y., Taunton, J., Blanchard, S.C., mRNA decoding in human is kinetically and structurally distinct from bacteria. Nature 617(7959), 200-207 (2023).

37. Cech, T.R., The ribosome is a ribozyme. Science 289, 878–879 (2000).

38. Morgan, D.G., Ménétret, J.-F., Radermacher, M., Neuhof, A., Akey, I. V, Rapoport, T.A., Akey, C.W., A comparison of the yeast and rabbit 80S ribosome reveals the topology of the nascent chain exit tunnel, inter-subunit bridges and mammalian rRNA expansion segments. J. Mol. Biol. 301, 301–321 (2000).

39. Melnikov, S., Ben-Shem, A., Garreau de Loubresse, N., Jenner, L., Yusupova, G., Yusupov, M., One core, two shells: bacterial and eukaryotic ribosomes. Nat. Struct. Mol. Biol. 19, 560–567 (2012).

40. Laursen, B.S., Sorensen, H.P., Mortensen, K.K., and Sperling-Petersen, H.U., Initiation of Protein Synthesis in Bacteria. Microbiol. Mol. Biol. Rev. 69, 101–123 (2005).

41. Filbin, M. E., and Kieft, J. S., Toward a structural understanding of IRES RNA function. Current Opinion in Structural Biology 19, 267–276 (2009).
42. Shine, J., and Dalgarno, L., The 3’-terminal sequence of Escherichia coli 16S ribosomal RNA: complementarity to nonsense triplets and ribosome binding sites. Proc. Natl. Acad. Sci. U. S. A. 71, 1342–1346 (1974).
43. Wen, J.D., Kuo, S.T., Chou, H.D., The diversity of Shine-Dalgarno sequences sheds light on the evolution of translation initiation. RNA Biol. 18(11), 1489-1500 (2021).
44. Rodnina, M.V., Translation in Prokaryotes. Cold Spring Harb. Perspect. Biol. 10(9), a032664 (2018).
45. Jackson, R.J., Hellen, C.U.T., Pestova, T. V., The mechanism of eukaryotic translation initiation and principles of its regulation. Nat. Rev. Mol. Cell Biol. 11, 113–127 (2010).
46. Hinnebusch, A.G., and Lorsch, J.R., The mechanism of eukaryotic translation initiation: New insights and challenges. Cold Spring Harb. Perspect. Biol. 4, 011544 (2012).
47. Abaeva I.S., Vicens Q., Bochler A., Soufari H., Simonetti A., Pestova T.V., Hashem Y., Hellen C.U.T., The Halastavi árva Virus Intergenic Region IRES Promotes Translation by the Simplest Possible Initiation Mechanism. Cell Rep., 33(10), 108476 (2020).
48. Agirrezabala, X., and Frank, J., Elongation in translation as a dynamic interaction among the ribosome, tRNA, and elongation factors EF-G and EF-Tu. Q. Rev. Biophys. 42, 159–200 (2009).
49. Fu, Z., Indrisiunaite, G., Kaledhonkar, S., Shah B., Sun M., Chen B., Grassucci R.A., Ehrenberg M., Frank J., The structural basis for release-factor activation during translation termination revealed by time-resolved cryogenic electron microscopy. Nat. Commun. 10, 2579 (2019)

50. Zafar, H., Hassan, A. H., Demo, G., Translation machinery captured in motion. WIREs RNA, e1792 (2023).

51. Zavialov, A. V, Mora, L., Buckingham, R.H., Ehrenberg, M., Release of peptide promoted by the GGQ motif of class 1 release factors regulates the GTPase activity of RF3. Mol. Cell 10, 789–798 (2002).

52. Song, H., Mugnier, P., Das, A.K., Webb, H.M., Evans, D.R., Tuite, M.F., Hemmings, B.A., Barford, D., The crystal structure of human eukaryotic release factor eRF1--mechanism of stop codon recognition and peptidyl-tRNA hydrolysis. Cell 100(3), 311-321 (2000).

53. Cheng, Z., Saito, K., Pisarev, A.V., Wada, M., Pisareva, V.P., Pestova, T.V., Gajda, M., Round, A., Kong, C., Lim, M., Nakamura, Y., Svergun, D.I., Ito, K., Song, H., Structural insights into eRF3 and stop codon recognition by eRF1. Genes Dev. 23(9), 1106-1118 (2009).

54. Mantsyzov, A.B., Ivanova, E.V., Birdsall, B., Alkalaeva, E.Z., Kryuchkova, P.N., Kelly, G., Frolova, L.Y., Polshakov ,V.I., NMR solution structure and function of the C-terminal domain of eukaryotic class 1 polypeptide chain release factor. FEBS J. 277(12), 2611-2627 (2010).

55. Kong, C., Ito, K., Walsh, M.A., Wada, M., Liu, Y., Kumar, S., Barford, D., Nakamura, Y., Song, H., Crystal structure and functional analysis of the eukaryotic class II release factor eRF3 from S. pombe. Mol. Cell. 14(2), 233-245 (2004).

56. Zavialov, A. V, Hauryliuk, V. V, Ehrenberg, M., Splitting of the Posttermination Ribosome into Subunits by the Concerted Action of RRF and EF-G. Mol. Cell 18, 675–686 (2005).

57. Peske, F., Rodnina, M. V, Wintermeyer, W., Sequence of Steps in Ribosome Recycling as Defined by Kinetic Analysis. Mol. Cell 18, 403–412 (2005).

58. Pisarev, A. V., Skabkin, M.A., Pisareva, V.P., Skabkina, O. V., Rakotondrafara, A.M., Hentze, M.W., Hellen, C.U.T., Pestova, T. V., The Role of ABCE1 in Eukaryotic Posttermination Ribosomal Recycling. Mol. Cell 37, 196–210 (2010).
59. Becker, T., Franckenberg, S., Wickles, S., Shoemaker, C.J., Anger, A.M., Armache, J.-P., Sieber, H., Ungewickell, C., Berninghausen, O., Daberkow, I., Karcher, A., Thomm, M., Hopfner, K.P., Green, R., and Beckmann, R., Structural basis of highly conserved ribosome recycling in eukaryotes and archaea. Nature 482, 501–506 (2012).
60. Kratzat, H., Mackens-Kiani, T., Ameismeier, M., Potocnjak, M., Cheng, J., Dacheux , E., Namane, A., Berninghausen, O., Herzog, F., Fromont-Racine, M., Becker, T., Beckmann, R., A structural inventory of native ribosomal ABCE1-43S pre-initiation complexes. EMBO J. 40(1):e105179 (2021).
61. Dong, J., Lai, R., Nielsen, K., Fekete, C.A., Qiu, H., Hinnebusch, A.G., The essential ATP-binding cassette protein RLI1 functions in translation by promoting preinitiation complex assembly. J. Biol. Chem. 279(40), 42157-42168 (2004).
62. Chen, Z.Q., Dong, J., Ishimura, A., Daar, I., Hinnebusch, A.G., Dean, M., The essential vertebrate ABCE1 protein interacts with eukaryotic initiation factors. J. Biol. Chem. 281(11), 7452-7457 (2006).
63. Prydderch, M.L., Waltham, N.J., Turchetta, R., French, M.J., Holt, R., Marshall, A., Burt, D., Bell, R., Pool, P., Eyles, C., Mapson-Menard, H., A 512×512 CMOS Monolithic Active Pixel Sensor with integrated ADCs for space science. Nucl. Inst. and Meth. in Phy. Res. Sec. A: Accelerators, Spectrometers, Detectors and Associated Equipment, 512(1–2), 358-367 (2003).

64. Bai, X., Fernandez, I., McMullan, G., Scheres, S., Ribosome structures to near-atomic resolution from thirty thousand cryo-EM particles. eLife 2, e00461 (2013).

65. Liao, M., Cao, E., Julius, D., Cheng, Y., Structure of the TRPV1 ion channel determined by electron cryo-microscopy. Nature 504, 107–112 (2013).

66. Cao, E., Liao, M., Cheng, Y., Julius, D., TRPV1 structures in distinct conformations reveal activation mechanisms. Nature 504, 113–118 (2013).

67. Henderson, R., and Glaeser, R.M., Quantitative analysis of image contrast in electron micrographs of beam-sensitive crystals. Ultramicroscopy 16, 139–150 (1985).

68. Glaeser, R., Retrospective: radiation damage and its associated "information limitations". J. Struct. Biol. 163, 271–276 (2008).

69. Brilot, A., Chen, J., Cheng, A., Pan, J., Harrison, S., Potter, C., Carragher, B., Henderson, R., Grigorieff, N., Beam-induced motion of vitrified specimen on holey carbon film. J. Struct. Biol. 177, 630–637 (2012).

70. McMullan, G., Chen, S., Henderson, R., Faruqi, A.R., Detective quantum efficiency of electron area detectors in electron microscopy. Ultramicroscopy 109(9), 1126-1143 (2009).

71. Campbell, M.G., Cheng, A., Brilot, A.F., Moeller, A., Lyumkis, D., Veesler, D., Pan, J., Harrison, S.C., Potter S.C., Carragher B., Grigorieff N., Movies of Ice-Embedded Particles Enhance Resolution in Electron Cryo-Microscopy. Structure 20(11), 1823-1828 (2012).

72. Li, X., Mooney, P., Zheng, S., Booth, C., Braunfeld, M., Gubbens, S., Agard, D., Cheng, Y., Electron counting and beam-induced motion correction enable near-atomic-resolution single-particle cryo-EM. Nat. Methods 10, 584–590 (2013).

73. Scheres, S., Beam-induced motion correction for sub-megadalton cryo-EM particles. eLife 3, e03665 (2014).

74. Fukuda, Y., Stapleton K., Kato T., Progress in spatial resolution of structural analysis by cryo-EM. Microscopy 72(2), Pages 135-143 (2023).

75. Murata, K., and Wolf, M., Cryo-electron microscopy for structural analysis of dynamic biological macromolecules. Biochim. Biophys. Acta. Gen. Subj. 1862(2), 324-334 (2018).

76. Henzler-Wildman, K., Kern, D., Dynamic personalities of proteins. Nature 450, 964–972 (2007).

77. Fu, Z., Kaledhonkar, S., Borg, A., Sun, M., Chen, B., Grassucci, R.A., Ehrenberg, M., Frank, J., Key Intermediates in Ribosome Recycling Visualized by Time-Resolved Cryoelectron Microscopy. Structure 24(12), 2092-2101 (2016).

78. Nauman, J.V., Campbell, P.G., Lanni, F., Anderson, J.L., Diffusion of insulin-like growth factor-I and ribonuclease through fibrin gels. Biophys. J. 92(12),4444-4450 (2007).

79. Walker, M., Trinick, J., White, H., Millisecond time resolution electron cryo-microscopy of the M-ATP transient kinetic state of the acto-myosin ATPase. Biophys. J. 68(4), 8S-91 (1995).

80. Dandey, V.P., Wei, H., Zhang, Z., Tan, Y.Z., Acharya, P., Eng, E.T., Rice, W.J., Kahn, P.A., Potter, C.S., Carragher, B., Spotiton: New features and applications. J. Struct. Biol. 202(2), 161-169 (2018).

81. Dandey, V.P., Budell, W.C., Wei, H., Bobe, D., Maruthi, K., Kopylov, M., Eng, E.T., Kahn, P.A., Hinshaw, J.E., Kundu, N., Nimigean, C.M., Fan, C., Sukomon, N., Darst, S.A., Saecker, R.M., Chen, J., Malone, B., Potter, C.S., Carragher, B., Time-resolved cryo-EM using Spotiton. Nat. Methods 17, 897–900 (2020).

82. White, H.D., Walke,r M.L., Trinick, J., A computer-controlled spraying-freezing apparatus for millisecond time-resolution electron cryomicroscopy. J. Struct. Biol. 121(3),306-313 (1998).

83. Bernardinelli, Y., Haeberli, C., Chatton, J.-Y., Flash photolysis using a light emitting diode: An efficient, compact, and affordable solution. Cell Calcium 37(6), 565-572 (2005).

84. Shaikh, T.R., Barnard, D., Meng, X., Wagenknecht, T., Implementation of a flash-photolysis system for time-resolved cryo-electron microscopy. J. Struct. Biol. 165(3), 184-189 (2009).

85. Yoder, N., Jalali-Yazdi, F., Noreng, S., Houser, A., Baconguis, I., Gouaux E., Light-coupled cryo-plunger for time-resolved cryo-EM. J. Struct. Biol. 212(3), 107624 (2020).

86. Romero, A.M., Bonin, C., Twomey, E.C., Time-Resolved Cryo-EM Specimen Preparation with Single Millisecond Precision. Biorxiv (2023) doi: https://doi.org/10.1101/2023.08.24.554704

87. Heymann, J.B., Conway, J.F., Steven, A.C., Molecular dynamics of protein complexes from four-dimensional cryo-electron microscopy. J. Struct. Biol. 147(3), 291-301 (2004).

88. Mandelkow, E.M., Mandelkow, E., Milligan, R.A., Microtubule dynamics and microtubule caps: a time-resolved cryo-electron microscopy study. J. Cell Biol. 114(5), 977-991 (1991).

89. D'Imprima, E., Floris, D., Joppe, M., Sánchez, R., Grininger, M., Kühlbrandt, W.,Protein denaturation at the air-water interface and how to prevent it. eLife 8, e4274 (2019).

90. Glaeser, R.M., Proteins, interfaces, and cryo-EM grids. Curr. Opin. Colloid Interface Sci. 34, 1-8 (2018).

91. Feng, X., Fu, Z., Kaledhonkar, S., Jia, Y., Shah, B., Jin, A., Liu, Z., Sun, M., Chen, B., Grassucci, R.A., Ren, Y., Jiang, H., Frank, J., Lin, Q., A Fast and Effective Microfluidic Spraying-Plunging Method for High-Resolution Single-Particle Cryo-EM. Structure 25(4), 663-670 (2017).
92. Torino, S., Dhurandhar, M., Stroobants, A., Claessens, R., Efremov, R.G., Time-resolved cryo-EM using a combination of droplet microfluidics with on-demand jetting. Nat. Methods 20, 1400-1408 (2023).
93. Bhattacharjee, S., Feng, X., Maji, S., Dadhwal, P., Zhang, Z., Brown, Z.P., Frank J., Time resolution in cryo-EM using a PDMS-based microfluidic chip assembly and its application to the study of HflX-mediated ribosome recycling. Cell (2024) in press
94. Courson, R., Fouet, M., Joseph, P., Mesnilgrente, F., Conédéra, V., Gué, A.M., SAMs vapor deposition: A ready to use functionalization technology for monitoring wettability properties in microfluidic devices. The 18th Intl. Conf. on Mini. Sys. for Chem. and Life Sci. MicroTAS 2014, San Antonio, United States.
95. Gutell, R.R., Cannone, J.J., Konings, D., Gautheret, D., Predicting U-turns in ribosomal RNA with comparative sequence analysis. J. Mol. Biol. 300(4), 791-803 (2003).
96. Kryuchkova, P., Grishin, A., Eliseev, B., Karyagina, A., Frolova, L., Alkalaeva, E., Two-step model of stop codon recognition by eukaryotic release factor eRF1. Nucleic Acids Res. 41(8), 4573-4586 (2013).
97. Scolnick, E., Tompkins, R., Caskey, T., Nirenberg, M., Release factors differing in specificity for terminator codons. Proc. Natl. Acad. Sci. USA 61(2), 768-774 (1996).
98. Seit-Nebi, A., Frolova, L., Kisselev, L., Conversion of omnipotent translation termination factor eRF1 into ciliate-like UGA-only unipotent eRF1. EMBO Rep. 3(9), 881-886 (2002).

99. Pisarev, A.V., Unbehaun, A., Hellen, C.U., Pestova, T.V., Assembly and analysis of eukaryotic translation initiation complexes. Methods Enzymol. 430, 147-177 (2007).

100. Potter, C.S., Chu, H., Frey, B., Green, C., Kisseberth, N., Madden, T.J., Miller, K.L., Nahrstedt, K., Pulokas, J., Reilein, A., Tcheng, D., Weber, D., Carragher, B., Leginon: a system for fully automated acquisition of 1000 electron micrographs a day. Ultramicroscopy 77(3-4), 153-161 (1999).

101. Scheres, S.H.W., RELION: Implementation of a Bayesian approach to cryo-EM structure determination., J. Struct. Biol. 180(3), 519-530 (2012).

102. Zivanov, J., Nakane, T., Forsberg, B.O., Kimanius, D., Hagen, W.J., Lindahl, E., Scheres, S.H., New tools for automated high-resolution cryo-EM structure determination in RELION-3. Elife 7, e42166 (2018).

103. Zivanov, J., Nakane, T., Scheres, S.H.W., Estimation of high-order aberrations and anisotropic magnification from cryo-EM data sets in RELION-3.1. IUCrJ 7, 253–267 (2020).

104. Zheng, S.Q., Palovcak, E., Armache, J.P., Verba, K.A., Cheng, Y., Agard, D.A.. MotionCor2: anisotropic correction of beam-induced motion for improved cryo-electron microscopy. Nat. Methods 14(4), 331-332 (2017).

105. Zhang, K., Gctf: Real-time CTF determination and correction. J. Struct. Biol. 193(1), 1-12 (2016).

106. Wagner, T., Merino, F., Stabrin, M., Moriya, T., Antoni, C., Apelbaum, A., Hagel, P, Sitsel, O., Raisch, T., Prumbaum, D., Quentin, D., Roderer, D., Tacke, S., Siebolds, B., Schubert, E., Shaikh, T.R., Lill, P., Gatsogiannis, C., Raunser, S., SPHIRE-crYOLO is a fast and accurate fully automated particle picker for cryo-EM. Commun. Biol. 19(2), 218 (2019).

107. Zivanov, J., Nakane, T., Scheres, S.H.W., A Bayesian approach to beam-induced motion correction in cryo-EM single-particle analysis. IUCrJ, 6, 5–17 (2019).

108. Pettersen, E.F., Goddard, T.D., Huang, C.C., Couch, G.S., Greenblatt, D.M., Meng, E.C., Ferrin, T.E., UCSF Chimera-a visualization system for exploratory research and analysis. J. Comput. Chem. 25(13), 1605-1612 (2004).

109. Liebschner, D., Afonine, P.V., Baker, M.L., Bunkóczi, G., Chen, V.B., Croll, T.I., Hintze, B., Hung, L.-W., Jain, S., McCoy, A.J., Moriarty, N.W., Oeffner, R.D., Poon, B.K., Prisant, M.G., Read, R.J., Richardson, J.S., Richardson, D.C., Sammito, M.D., Sobolev, O.V., Stockwell, D.H., Terwilliger, T.C., Urzhumtsev, A.G., Videau, L.L., Williams, C.J., Adams, P.D., Macromolecular structure determination using X-rays, neutrons and electrons: recent developments in Phenix. Acta Cryst. D 75, 861–877 (2019).

110. Emsley, P., Lohkamp, B., Scott, W.G., Cowtan, K., Features and development of Coot. Acta Crystallogr. D Biol. Crystallogr. 66(4), 486-501 (2010).

111. Goddard, T.D., Huang, C.C., Meng, E.C., Pettersen, E.F., Couch, G.S., Morris, J.H., Ferrin, T.E., UCSF ChimeraX: Meeting modern challenges in visualization and analysis. Protein Sci. 27(1), 14-25 (2018).

112. Fogler, H. S., Essentials of Chemical Reaction Engineering, 2nd ed. Upper Saddle River: Pearson Education (2010).

113. Afonine, P.V., Klaholz, B.P., Moriarty, N.W., Poon, B.K., Sobolev, O.V., Terwilliger, T.C., Adams, P.D., Urzhumtsev, A., New tools for the analysis and validation of cryo-EM maps and atomic models. Acta Crystallogr. D Struct. Biol. 74(9), 814-840 (2018).

114. Williams, C.J., Headd, J.J., Moriarty, N.W., Prisant, M.G., Videau, L.L., Deis, L.N., Verma, V., Keedy, D.A., Hintze, B.J., Chen, V.B., Jain, S., Lewis, S.M., Arendall, W.B. 3rd, Snoeyink, J., Adams, P.D., Lovell, S.C., Richardson, J.S., Richardson, D.C., MolProbity: More and better reference data for improved all-atom structure validation. Protein Sci. 27(1), 293-315 (2018).

115. Fischer, N., Neumann, P., Konevega, A.L., Bock, L.V., Ficner, R., Rodnina, M.V., Stark, H., Structure of the E. coli ribosome-EF-Tu complex at <3 Å resolution by Cs-corrected cryo-EM. Nature 520(7548), 567-70 (2015).

116. Schmeing, T.M., Voorhees, R.M., Kelley, A.C., Gao, Y.G., Murphy, F.V. 4th, Weir, J.R., Ramakrishnan, V., The crystal structure of the ribosome bound to EF-Tu and aminoacyl-tRNA. Science 326(5953), 688-694 (2009).

117. Voorhees, R.M., Ramakrishnan, V., Structural basis of the translational elongation cycle. Annu. Rev. Biochem. 82, 203-236 (2013).

118. Vetter, I.R., Wittinghofer, A., The guanine nucleotide–binding switch in three dimensions. Science 294, 1299-1304 (2001).

119. Pisareva, V.P., Pisarev, A.V., Hellen, C.U., Rodnina, M.V., Pestova, T.V., Kinetic analysis of interaction of eukaryotic release factor 3 with guanine nucleotides. J. Biol. Chem. 281(52), 40224-40235 (2006).